Master thesis : Multi-echo 23Na MRI Sequence Evaluation for Quantitative Mapping (including introduction to research methodology)

Auteur : Minne, Romane
Promoteur(s) : Phillips, Christophe
Faculté : Faculté des Sciences appliquées
Diplôme : Master en ingénieur civil biomédical, à finalité spécialisée
Année académique : 2025-2026
URI/URL : http://hdl.handle.net/2268.2/26149

University of Liège
Faculty of Applied Sciences
Academic Year 2025–2026

Multi-echo ^{23}Na MRI Sequence Evaluation for Quantitative Mapping

Thesis presented to obtain the Master's degree in Biomedical Engineering

Author:
Romane Minne

Supervisors:
Christophe Phillips
Mikhail Zubkov

June 2026

Acknowledgments

This Master's Thesis represents my first long-term research project as part of my studies in Biomedical Engineering. It has been a very rewarding experience, allowing me to work in a real research environment at the Cyclotron Research Center (CRC). Although I started this project with limited knowledge of sodium MRI, and MRI in general, I learned a great deal throughout this project and gained some experience. For this reason, I would like to express my gratitude to the people who contributed to the success of this work.

My sincere thanks go first to Mikhail Zubkov, who supported me throughout all stages of this project, from learning the fundamentals to the final revision of the report, including method development and data acquisition. He was always available to answer my questions and took the time to help me despite his busy schedule. I am also grateful for the opportunity he gave me to submit an abstract based on this work to the annual meeting of the European Society for Magnetic Resonance in Medicine and Biology (ESMRMB 2026).

Special thanks are also due to my academic supervisor, Christophe Phillips, for giving me the opportunity to work on such an interesting project. His guidance, advice, and support throughout the thesis were greatly appreciated. His feedback and availability played an important role in the completion of this work.

I am grateful to the members of my jury, Mikhail Zubkov, Christophe Phillips, Gilles Vandewalle, and Guillaume Drion, for their interest in this project and for taking the time to evaluate this work.

A special acknowledgment is also extended to all the members of the CRC. Working in such a stimulating research environment was really appreciated. I met many passionate and supportive people who were always willing to share their knowledge. Many discussions helped me to solve problems encountered during this project and made my time at the CRC particularly enjoyable.

Finally, my deepest thanks goes to my family for their constant support throughout my five years of university studies. Their encouragement and confidence gave me the strength to overcome challenges and complete this thesis. They always showed interest in my work and supported me throughout this journey, even when the scientific details were not always easy to understand.

Contents

List of Figures

List of Tables

Chapter 1

Introduction

1.1 Context and motivations

Sodium-23 Magnetic Resonance Imaging (^{23}Na MRI) is an imaging modality based on the same physical principles as conventional hydrogen (^{1}H) MRI, relying on nuclear magnetic resonance phenomena. One of the main advantages of both ^{1}H and ^{23}Na MRI techniques is that they are non-invasive and non-ionizing, in contrast to imaging modalities such as radiography, Computed Tomography (CT), Positron Emission Tomography (PET), or Single Photon Emission CT (SPECT) scans, which involve exposure to ionizing radiation for X-ray or radioactive nuclear decay.

Hydrogen MRI is widely used in clinical practice due to the high abundance of hydrogen in the human body, which is composed of approximately 60% water. This results in a strong signal and high signal-to-noise ratio (SNR), enabling detailed anatomical imaging. In addition to structural imaging, ^{1}H MRI can also provide functional and physiological information about various organs, including the brain, heart, lungs, kidneys, and soft tissues. The versatility of MRI is further improved by the availability of numerous pulse sequences, allowing for a wide range of clinical and research applications.

The development of MRI dates back to the early 1970s, followed by the first clinical ^{1}H MRI systems. Sodium MRI emerged shortly after, with initial studies performed on animal models in the early 1980s, followed by applications to human brain, cardiac, and abdominal imaging [1]. Early investigations demonstrated the potential of ^{23}Na MRI for detecting pathological conditions such as brain tumors and ischemia, due to its sensitivity to changes in tissue sodium concentration. However, the low SNR of sodium imaging limited the interest of scientists, leading to a halt in research on this topic.

During the 1990s, advances in hardware, including the development of high-field MRI systems (1.5T and 3T), improved radio-frequency (RF) coils, and faster imaging sequences, significantly enhanced sodium imaging capabilities. These technological improvements led to better spatial resolution and reduced acquisition times. From the 2000s to the present day, continued progress in MRI technology, including ultra-high-field (7T and above) systems and advanced reconstruction techniques, has further improved the achievable SNR and revived interest in sodium imaging for biomedical applications. Despite these advances, ^{23}Na MRI remains challenging due to its intrinsically low SNR. This limitation arises from several factors, including the lower gyromagnetic ratio of sodium compared to the one of hydrogen, its lower *in vivo* concentration, and its fast bi-exponential relaxation properties in biological tissues. These aspects will be discussed

in more details in the following of this introduction.

Today, although ^{23}Na MRI has demonstrated significant potential for assessing tissue viability, ion homeostasis, and metabolic changes, it is still not widely used in routine clinical practice and remains primarily a research tool. This is mainly due to persistent technical challenges, including low SNR, long acquisition times, and the need for specialized hardware and pulse sequences. These limitations, along with ongoing developments aimed at overcoming them, will be discussed later in this report.

1.2 Sodium as a biomarker of tissue viability

Sodium is a chemical element from the alkali metals. Its most common form is the isotope ^{23}Na, with an almost 100% natural abundance atom both in the human body and in nature [2]. This element is an indispensable component of life and plays a central role in maintaining cellular and systemic homeostasis. In the human body, most sodium lies in the extracellular fluid, mainly in blood plasma and the cerebrospinal fluid (CSF) in the brain, while the intracellular sodium is maintained at much lower levels. Table 1.1 regroups the mean concentrations of sodium in different parts in the body, as well as their longitudinal and transverse relaxation times at 3T [1].

Tissue	**[Na^+] (mM)**	**T_1 (ms)**	**$T_{2,\mathbf{fast}}$ (ms)**	**$T_{2,\mathbf{slow}}$ (ms)**
Brain				
WM	20–60	15–35	0.8–3	15–30
GM	30–70	15–35	0.8–3	15–30
CSF	140–150	50–55	–	55–65
Cartilage	250–350	15–25	0.5–2.5	10–30
Muscle	15–30	12–25	1.5–2.5	15–30

Table 1.1: Sodium concentrations and relaxation times for different tissues at 3T

Sodium is the most abundant extracellular cation, which is primarily responsible for the regulation of fluid balance and blood pressure. By controlling osmotic water movement, sodium determines extracellular fluid volume, influences blood volume, and directly affects arterial pressure. Kidney function is particularly sensitive to sodium levels in the blood, excessive sodium intake can impair the renal system, leading to an imbalance in fluid and electrolyte homeostasis [3].

In addition to its role in fluid regulation, sodium is indispensable for nerve impulse transmission. The rapid influx of Na^+ ions through voltage-gated sodium channels enables the generation and propagation of action potentials in neurons, thus allowing the transmission of electrical signals throughout the nervous system and across the body. Sodium also participates in muscle contraction mechanisms. The depolarization of muscle cell membranes, driven by sodium entry, triggers the release of calcium ions, which in turn initiate the contraction-relaxation cycle in skeletal, smooth, and cardiac muscle fibers. In the heart, this sodium-dependent process ensures the rhythmic contraction essential to cardiac function.

Furthermore, sodium contributes to the regulation of pH and ion homeostasis. Acting as a buffer in the blood, it maintains intracellular levels of pH and supports overall

acid–base balance. By modulating osmotic pressure, sodium controls water distribution between intracellular, interstitial, and intra-vascular compartments, ensuring good cellular function and hydration.

Therefore, ^{23}Na MRI has high potential in identifying disorders associated with ionic changes in *in vivo* images, complementing classic ^{1}H MRI that remains mostly an anatomical analysis.

Na^+/K^+-ATPase pump

Under physiological conditions, intracellular sodium concentration ranges approximately from 10 to 15 mM, when extracellular sodium concentration stands around 140-150 mM. There is, then, a huge concentration gradient between the two compartments, which is essential to maintain membrane excitability, osmotic balance and ion homeostasis. Any disruption of this precise balance can lead to an increase of the intracellular concentration. One of the main mechanisms used to effectively maintain this gradient is the Na^+/K^+-ATPase pump [4], illustrated in Figure 1.1. This membrane-associated protein complex actively transports three sodium ions out of the cell and two potassium ions into the cell, working against their electrochemical gradients.

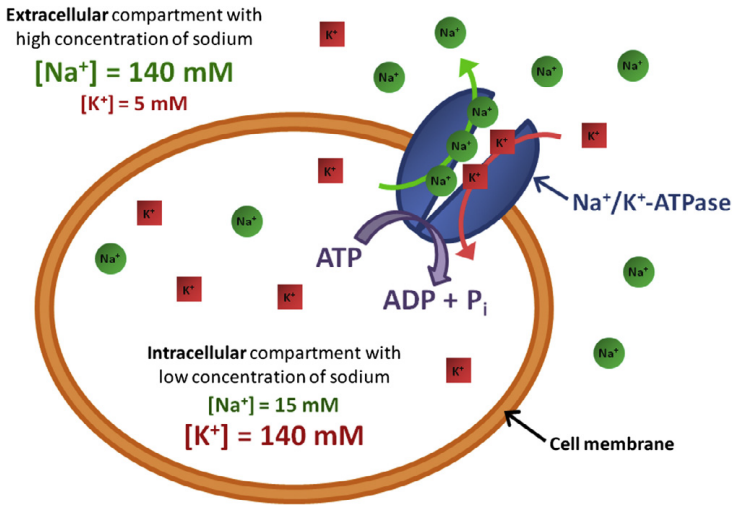

Figure 1.1: Na^+/K^+-ATPase pump mechanism

The main roles of the Na^+/K^+-ATPase pump are to maintain physiological Na^+ and K^+ gradients, to generate and stabilize the resting membrane potential and to prevent osmotic swelling and the potential lysis of the cell.

The preservation of this electrochemical gradient is critical for normal tissue function. Neuronal communication, muscle contraction and many other mechanisms rely directly on sodium motion across biological membranes. Disturbances in sodium homeostasis are often associated with pathological problems such as cellular injury, metabolic failure, inflammation, ischemia, etc., leading to the accumulation of sodium within tissues.

Sodium can then be used as an promising biomarker because it reflects cellular viability and metabolic state. In fact, ^{23}Na MRI provides valuable information about physiological and biochemical processes occurring at the cell level, in contrast to conventional ^{1}H MRI that is primarily used to show anatomical and structural alterations. Changes in sodium

concentration may then appear before structural damages becomes visible in hydrogen MRI, making sodium MRI a good candidate for early disease detection and monitoring.

1.3 Clinical relevance of Sodium MRI

Alterations in sodium homeostasis are associated with many pathological processes. Because sodium gradients directly depend on membrane integrity and ATP availability, changes in Na^+ concentration constitute sensitive markers of metabolic dysfunction, tissue injury, and extracellular matrix (ECM) disorders. In this context, sodium MRI represents a valuable imaging modality for detecting early and subtle physiological changes that often remain undetectable with conventional imaging technique. Several clinical applications will be illustrated to show the diagnostic potential of ^{23}Na MRI.

1.3.1 Brain applications

In this section, three applications of ^{23}Na imaging are presented, including ischemic stroke, multiple sclerosis and brain tumors.

Ischemic stroke

In ischemic stroke, the interruption of blood flow leads to a reduction in oxygen and glucose supply, which impairs cellular energy production. The resulting ATP depletion rapidly induce failure of the Na^+/K^+-ATPase pump. This is characterized by a marked intracellular sodium accumulation within minutes after the onset of ischemia because the ionic gradients are no longer maintained. This increase occurs before structural abnormalities become visible on hydrogen MRI, making sodium MRI particularly relevant for the early detection of cytotoxic edema and metabolic impairment.

Figure 1.2 illustrates an example of hydrogen and sodium MR images of the same patient suffering of ischemic stroke [5]. As expected, sodium image provides especially higher sodium concentration in the region of the lesion and is quite easier to detect compared with the conventional FLAIR image. This suggests that sodium MRI may provide valuable information about tissue viability and the extent of irreversible damages during a stroke.

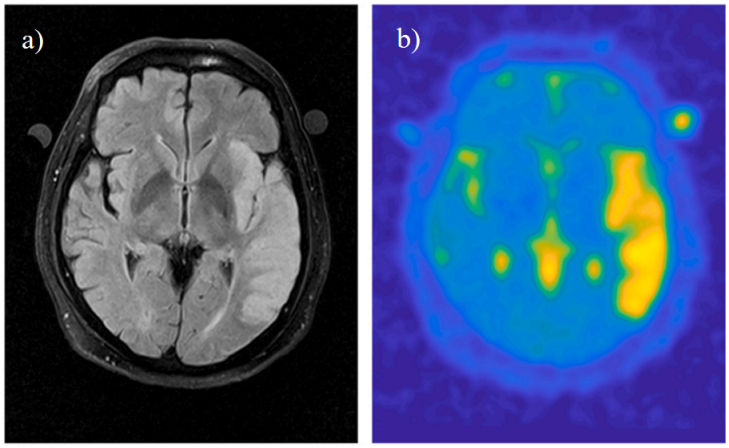

Figure 1.2: Ischemic stroke imaging example: a) ^{1}H FLAIR image and b) ^{23}Na MR image

Multiple sclerosis

Another application of sodium imaging can be neurodegenerative disorders such as multiple sclerosis. Multiple sclerosis induces inflammatory processes and demyelination, affecting both white and gray matter structures. It results in abnormal sodium accumulation in lesions as well as in apparently normal tissues, which potentially reflects metabolic dysfunction and axonal injury. This would reduce the efficiency of ionic regulation mechanisms, especially the activity of the Na^+/K^+-ATPase pump.

An example of comparison between hydrogen and sodium imaging on a multiple sclerosis patient is illustrated in Figure 1.3 [6]. As previously exposed, total sodium concentration (TSC), represented in Figure 1.3d, had increased in the region affected by the disease, when ^1H MR image does not provide any clear visual information about the location of the problematic region.

Sodium MRI may therefore provide complementary information by revealing metabolic abnormalities that are not detectable using standard imaging techniques.

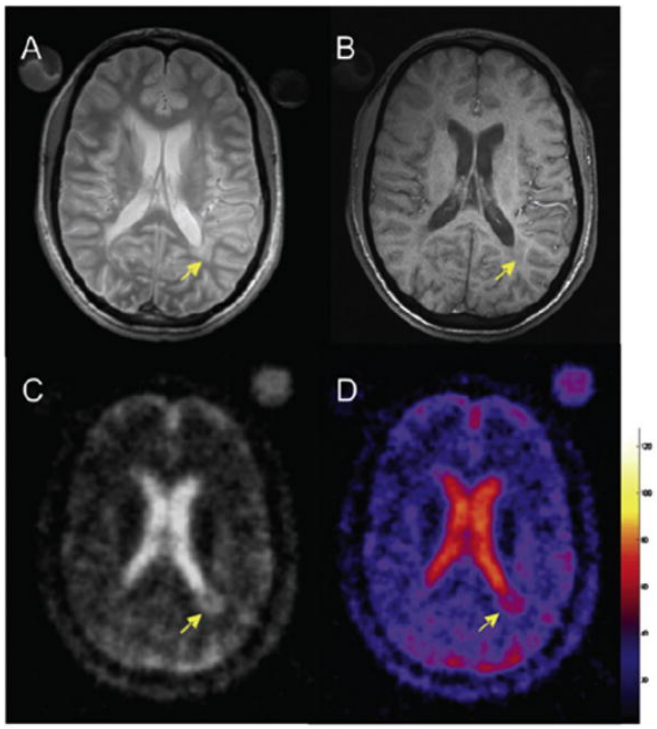

Figure 1.3: Multiple sclerosis imaging example: A) Proton density MRI, B) T1 weighted MRI, C) sodium MRI, and D) corresponding TSC map

Brain tumors

The last example of brain application of sodium MRI is brain tumors. Indeed, elevated sodium concentration are exhibited due to increased cellular proliferation, altered membrane permeability and the presence of necrotic components. Sodium levels have been shown to be correlate with tumor grade, metabolic activity, and therapeutic response.

Figure 1.4 represents two MR images, both with hydrogen and sodium human imaging [7]. Once again, higher sodium concentration around the tumoral region is observed on sodium MR image.

As a result, sodium MRI can also be considered as a promising tool for treatment monitoring, as metabolic changes may become detectable before anatomical modifications can be observed with hydrogen MRI using some contrast agent such as gadolinium.

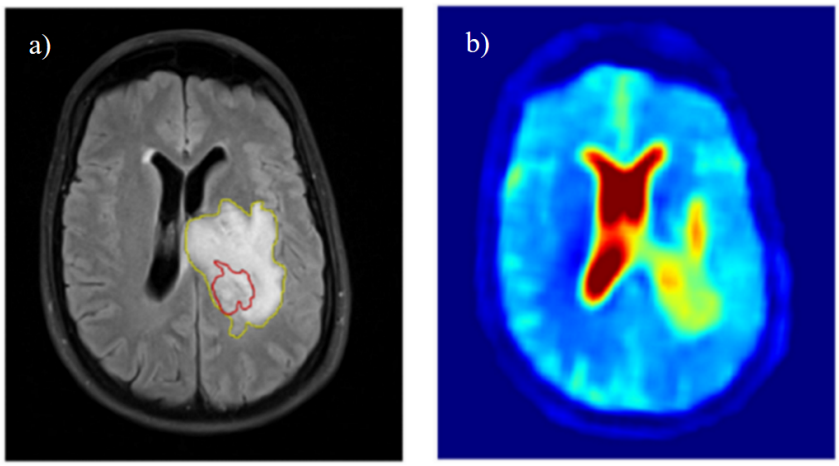

Figure 1.4: Brain tumor imaging example: a) T_2-weighted FLAIR imaging after application of Gadolinium-based contrast agent and b) ^{23}Na MRI.

1.3.2 Non-brain applications

Sodium MRI can be used in other parts of the human body, such as heart or knee joints. Here are presented the case of muscle hypertension and cartilage applications.

Muscle and hypertension

As previously demonstrated, sodium plays a central role in muscle contraction. The Na^+/K^+-ATPase pump maintains the electrochemical gradient across cell membranes, while the generation of an action potential induces rapid Na^+ influx into the cell and K^+ efflux toward the extracellular space. Several pathological conditions, including diabetes, starvation, and hypertension, are associated with altered Na^+/K^+-ATPase function. Sodium imaging therefore offers an alternative way to investigate these disorders.

Hypertension is a good example of sodium MRI application in muscular tissues. It has been shown that tissue sodium content differs between young subjects and older patients with hypertension. Some results are illustrated in Figure 1.5 [1]. A clear increase in sodium concentration is observed in hypertensive subjects. ^{23}Na MRI could then be used to monitor long-term cardiovascular risk caused by hypertension.

Cartilage

Cartilage is found in joints, ears, nose, and intervertebral discs, where it plays an essential structural and mechanical role. It is mainly composed of collagen fibers, proteoglycans, and water.

One important application of sodium imaging in cartilage concerns osteoarthritis, which is the most common form of arthritis, especially in older people. Currently, osteoarthritis is mainly evaluated using radiography, where the distance between adjacent bones is measured to follow cartilage loss, so the cartilage itself is not directly visualized. However, sodium concentration in cartilage has been shown to strongly correlate with fixed charge density and glycosaminoglycans (GAG) content, which attract and bound sodium ions [1]. ^{23}Na MRI therefore has strong potential for detecting cartilage loss at early stages of osteoarthritis. Figure 1.6 presents an example of cartilage sodium concentration mapping, where sodium content is clearly lower in osteoarthritis patient than in control subject, confirming the utility of sodium imaging.

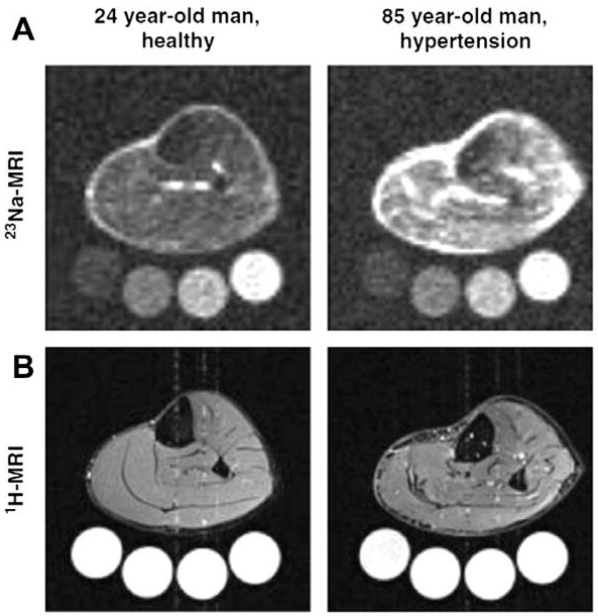

Figure 1.5: Hypertension imaging example of a healthy and hypertension patient: a) ^{23}Na MR image and b) corresponding ^{1}H MR image

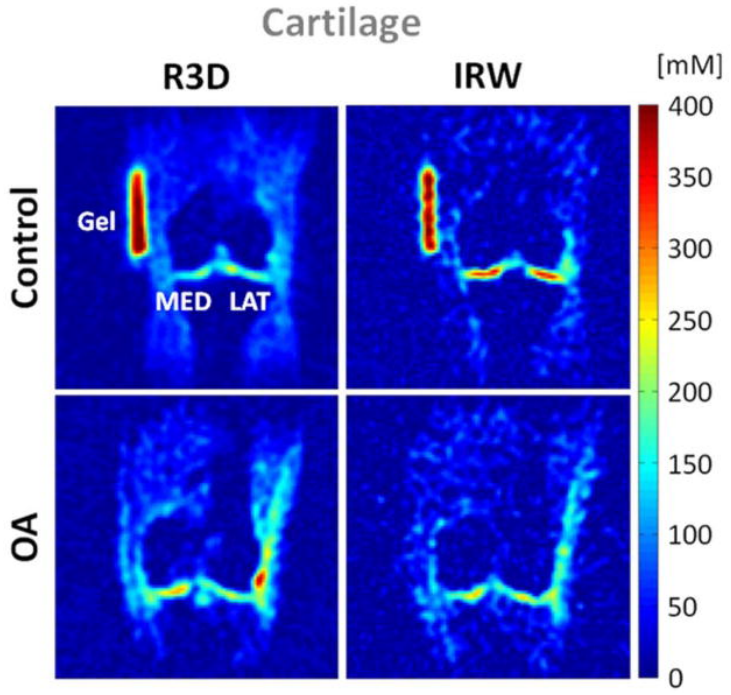

Figure 1.6: Cartilage imaging example: sodium concentration maps for control and osteoarthritis patient using 3D radial (R3D) and IR WURST (IRW) sequences

Overall, sodium distribution provides valuable information regarding cellular viability, metabolic status, ECM composition and tissue organization. ^{23}Na MRI enables these ionic alterations to be assessed *in vivo* and offers complementary physiological information beyond conventional ^{1}H imaging. Consequently, robust determination of ^{23}Na concentration is critical, especially regarding the discrimination between intracellular and extracellular concentrations.

1.4 Magnetic Resonance Imaging

1.4.1 Hardware of MRI

The precise hardware of different MRI machines can differ from one to another. In general, it is composed of a main magnet, gradient system, radio-frequency (RF) system, control electronics and viewing console.

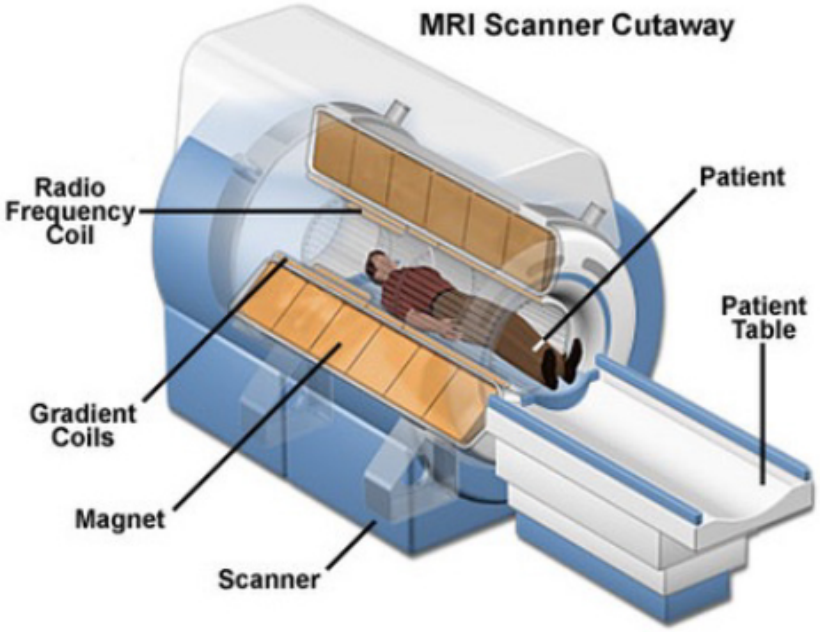

Figure 1.7: MRI hardware

The main magnet for high and ultra-high field MRI is a superconductor magnet composed of multiple shielded solenoidal coils. It is used to generate the large static magnetic field B_0 in one direction. In order to make the wires superconducting, a cryogenic system made of liquid helium is used to keep the wires cold enough.

In the end-part of the gradient system, the gradient coil produces linear gradient magnetic fields that are superposed to B_0. Three different coils exist for each direction of space, the x, y and z coils. The global magnetic field can be written as:

$$\mathbf{B} = (B_0 + xG_x + yG_y + zG_z)\hat{z} \tag{1.1}$$

where B_0 is the amplitude of B_0 in the z direction, $\hat{z}$ is the unit vector of the z axis, G_x, G_y and G_z are the gradient amplitudes in each spatial directions. These gradient coils are used to linearly modify B_0 over space, allowing spatial encoding.

The RF coils are the antennas used to emit the excitation RF power and receive the MR signal. In most MRI systems, separate coils are used for transmission and reception, although some designs combine both functions within a single coil. The geometry and design of the RF coils depend on the anatomical region being imaged and on the nucleus of interest. For example, specific RF coils are required for sodium MRI because of the difference in Larmor frequency of ^{23}Na compared to ^{1}H .

During transmission, the RF coil generates an oscillating magnetic field B_1^+ perpendicular to the static magnetic field B_0. This field excites the spins and moves the magnetization away from its equilibrium position. However, RF transmission also produces electric fields within the tissue, resulting in energy absorption and tissue heating. This effect is quantified by the specific absorption rate (SAR), defined as the RF power absorbed per unit mass of tissue and expressed in W/kg [8]. According to the IEC 60601-2-33 standard, the whole-body SAR is limited to 2 W/kg in normal operating mode and 4 W/kg in first-level controlled mode, while the head SAR must remain below 3.2 W/kg for both operating modes [9].

SAR represents an important safety constraint in MRI, particularly at ultra-high magnetic field strengths such as 7T, where larger RF power levels may be required to achieve the desired flip angles. Excessive SAR may lead to tissue heating and therefore limits the allowable sequence parameters, including repetition time and flip angle. Consequently, SAR must be carefully monitored and controlled during MRI acquisitions to ensure patient safety.

1.4.2 1-Hydrogen MRI

Classic ^{1}H magnetic resonance imaging is much simpler than the ^{23}Na one, even if the principle is the same. ^{1}H MRI is based on the behavior of the hydrogen spins, when exposed to external magnetic fields. In fact, hydrogen has a nuclear spin of 1/2, leading to 2 distinct levels of energy when placed into an external static magnetic field B_0, parallel and anti-parallel to the main direction of B_0. This distinction in energy levels allows the magnetic moment μ of atoms to create the macroscopic magnetization.

First, when the tissue is outside of any strong magnetic field, the total magnetization of the atoms caused by the microscopic distribution of hydrogen nuclear spins is globally zero due to their random orientations. Then, a strong, static and weakly alternative magnetic field B_0 is applied, leading to the polarization and reorganization of nuclear spins into the 2 energy levels, up and down, with some higher fraction of atoms up than down. It results in a net longitudinal magnetization $M_z = M_0$ in the direction of B_0. The magnetization, when perturbed from its equilibrium state, precesses around the direction of B_0 at the Larmor frequency:

$$\omega_0 = \gamma B_0 \tag{1.2}$$

where ω_0 is the Larmor frequency and γ is the gyromagnetic ratio.

However, the transverse magnetization, M_{xy}, in the xy-plane, is still equal to zero. In MRI, the signal measured by the receiver coil is originated from the transverse magnetization, which is formed through the nuclear spin phase coherence in the transverse plan. Applying B_1^+, a weak magnetic field, is then used to introduce a perturbation of the previous equilibrium. In a general manner, B_1^+ is in the range of the mT. The angle by which the magnetization is rotated is referred to as the flip angle (FA). It depends on both the amplitude and duration of the applied RF pulse. For example, a 90° pulse rotates the magnetization entirely into the transverse plane, when a 180° pulse totally inverts the longitudinal magnetization.

The frequency of the generated RF pulse needs to coincide with the Larmor frequency, such as $\omega_{RF} = \omega_0$. It creates the resonance condition, resulting in the rotation of M_z from the z-axis to the xy-plane, and thus the rise of M_{xy} because the spins precess at ω_0 and with

coherent phases in the xy-plane. The total macroscopic magnetization $\mathbf{M}(t)$ is a function of its components in each direction of the plane, such that $\mathbf{M}(t) = (M_{xy}(t), M_z(t))$.

1.4.3 Physics of 23 sodium MRI

Gyromagnetic ratio

The gyromagnetic ratio is a fundamental physical constant, which links the magnetic moment to the angular momentum of a nucleus:

$$\mu = I\gamma \tag{1.3}$$

where μ is the magnetic moment, I is the nuclear angular momentum and γ is the gyromagnetic ratio. The gyromagnetic ratio of sodium is $\gamma_{Na} = 11.262$ MHz/T, which is approximately 25% of the one of hydrogen, which is $\gamma_H = 42.577$ MHz/T. This lower value induces lower resonant frequency and consequently reduces the signal intensity in ^{23}Na MRI.

Nuclear spin and quadrupolar moment

The nuclear spin of ^{23}Na is $I = 3/2$ while the one of hydrogen is $I = 1/2$. As a consequence, ^{23}Na possesses a nuclear electric quadrupole moment that interacts with local electric field gradients (EFG) produced by the surrounding molecular environment. Therefore, in a magnetic field, the sodium nucleus has four Zeeman levels of energy: $-\frac{3}{2}, -\frac{1}{2}, +\frac{1}{2}$ and $+\frac{3}{2}$ [1].

The four energy levels allow to three transitions. The transition between $m_I = -\frac{1}{2}$ and $+\frac{1}{2}$ is referred as the central transition, while the transitions between $m_I = -\frac{3}{2}$ and $-\frac{1}{2}$, and between $+\frac{1}{2}$ and $+\frac{3}{2}$, are known as the satellite transitions.
Typically, only the central transition is narrow enough to be detectable *in vivo* under fast motional conditions. The satellite transitions are significantly broadened by quadrupolar interactions and are often outside of the bandwidth available by the machine.

As any nucleus with $I > \frac{1}{2}$, the nuclear charge distribution is asymmetric and can interact with the EFG. This non-spherical distribution gives rise to an electric quadrupole moment Q. The interactions of the electrons cloud with the EFG is the reason why quadrupolar coupling exists in ^{23}Na MRI.

1.4.4 Sodium relaxation properties

Here, the two main relaxation properties, the longitudinal and transverse ones, are described in order to better understand the physics of ^{23}Na MRI.

T_1 relaxation

The longitudinal relaxation time T_1 is representative of the relative time it takes the sodium nuclei to realign with B_0 in the z direction after an excitation. In other words, it determines the speed of M_z regrowth after the RF pulse. This relationship can be approximated by a mono-exponential asymptotic recovery. The equation 1.4 governs the evolution of the mono-exponential longitudinal magnetization as a function of time.

$$M_z(t) = M_0(1 - e^{-t/T_1}) \tag{1.4}$$

Different T_1 relaxation times lead to a different exponential recovery. The larger the T_1, the slower the recovery of M_z. Consequently, T_1 in sodium MRI is much shorter than in ^{1}H MRI due to the quadrupolar interactions.

T_2^* relaxation

The T_2 relaxation time describes the loss of phase coherence between nuclear spins after the excitation by the RF pulse, representing the decay of the transverse component M_{xy}. At the same time, the external magnetic field inhomogeneities impact the apparent value of the decay, which can be described by another time constant T_2'. The combined effect of these two phenomena is represented by T_2^*, which is the apparent transverse relaxation time. The following equation describes the relationship between these transverse relaxation times:

$$\frac{1}{T_2^*} = \frac{1}{T_2} + \frac{1}{T_2'} \tag{1.5}$$

Naturally, T_2^* is always smaller than T_2 because it is almost impossible to eliminate all the inhomogeneities of B_0.

Because sodium has a quadrupolar moment, its transverse relaxation phenomenon is dominated by interactions between the quadrupole moment and local electric field gradients. The strength and dynamics of these interactions depend on the molecular motion of ions in their environment [1].

In rapidly tumbling environments such as CSF and blood plasma, motional averaging partially cancels quadrupolar interactions. Indeed, the nuclei of sodium are free to move, making the relaxation times longer. Transverse relaxation decay can be considered as mono-exponential over time in these structures and can be expressed through the equation 1.6.

$$M_{xy}(t) = M_0\, e^{-t/T_2^*} \tag{1.6}$$

In restricted or semi-solid environments, corresponding to brain tissues, cartilage or muscles, a strong quadrupolar coupling is observed, leading to a fast decaying signal and very short relaxation components are expected. The motion of ions are restricted into these environments, which means that the quadrupolar interaction won't be canceled out as it was for liquid like environments.

As the commonly available imaging resolutions do not allow spatially resolving areas of restricted and free motion, the observed relaxation decay in tissues becomes bi-exponential, composed of two main components: fast and slow relaxation times as expressed in equation 1.7.

$$M_{xy}(t) = M_0(f e^{-t/T_{2,\mathtt{fast}}^*} + (1 - f)\, e^{-t/T_{2,\mathtt{slow}}^*}) \tag{1.7}$$

where M_0 is the initial transverse magnetization just after the RF pulse application, f is the signal fraction of the fast transverse relaxation time, t is the time, $T_{2,\mathtt{fast}}^*$ and $T_{2,\mathtt{slow}}^*$ are the fast and the slow relaxation times, respectively.

Each of the relaxation components can be used to represent different populations of sodium. The fast relaxation time $T^*_{2,\texttt{fast}}$ mainly describes the relaxation behavior of intracellular and restricted sodium atoms while the slow relaxation time $T^*_{2,\texttt{slow}}$ corresponds to lowly bounded and sodium presents in the extracellular space that are freer to move. It is important to note that there is no distinct separation between these two populations.

Table 1.1 regroups different values of relaxation times in the body. When compared to the relaxation times of hydrogen, these values are short, mean T_2^* hydrogen values for the gray matter and white matter are 66 and 53 ms at 3T, respectively [10]. That's why the use the ultra-short echo times to record the signal before it vanishes is essential (see section 1.4.5).

In general, the choice of the decay model will depend on the analyzed structure. As previously indicated, a bi-exponential approach to model the signal is considered in brain tissues, and a mono-exponential model is used to model the CSF sodium atoms behavior. However, some models have tri-exponential behavior, for example in the cartilage, where the ionic motion is even more restricted than in tissues. This tri-exponential model won't be used during this work.

1.4.5 Sequences and k-space sampling

A pulse sequence defines the timing and organization of all events occurring during an MRI acquisition. It describes when RF pulses are applied to excite the spins, when magnetic field gradients are switched on for spatial encoding, and when the MR signal is sampled. The choice of pulse sequence directly influences image contrast, acquisition time, SNR and the ability to characterize relaxation phenomena. Consequently, pulse sequence design is a key aspect of quantitative sodium MRI and should be designed with care.

The problem of sodium MRI is that most of the signal decays before it can be recorded, which is especially true for the fast component of T_2^*, if traditional pulse sequences are used. It leads to a very low SNR and a poor image quality. To tackle it, ultrashort echo times (UTE) sequences must be used to be able to acquire this very short decay of signal. UTE sequences are then really useful in capturing the fast T_2^* component.

The principle of a multi-echo UTE sequence is that several images are acquired at different echo times during the same scan. Each of them is a representation of the sodium content at different moments of the relaxing signal, allowing to trace the relaxation curve determined by equations 1.6 and 1.7.

Figure 1.8 illustrates an example of multiple UTE sequence acquisition [11]. The first images from the first echoes effectively represents the mixture of extra- and intracellular sodium while the later echoes mostly represent the extracellular content of sodium as the one presents in the CSF. It is then important to understand that both sodium populations are presents at the same time in the image, but with different intensities depending on the time elapsed after excitation.

Image formation in UTE sequences is performed through a process called radial encoding because the acquisition will always start at the center of k-space, where are located the lowest frequencies [12]. During radial encoding, the image is sampled in inverse Fourier space, or k-space, along different directions often referred to as projections. After enough

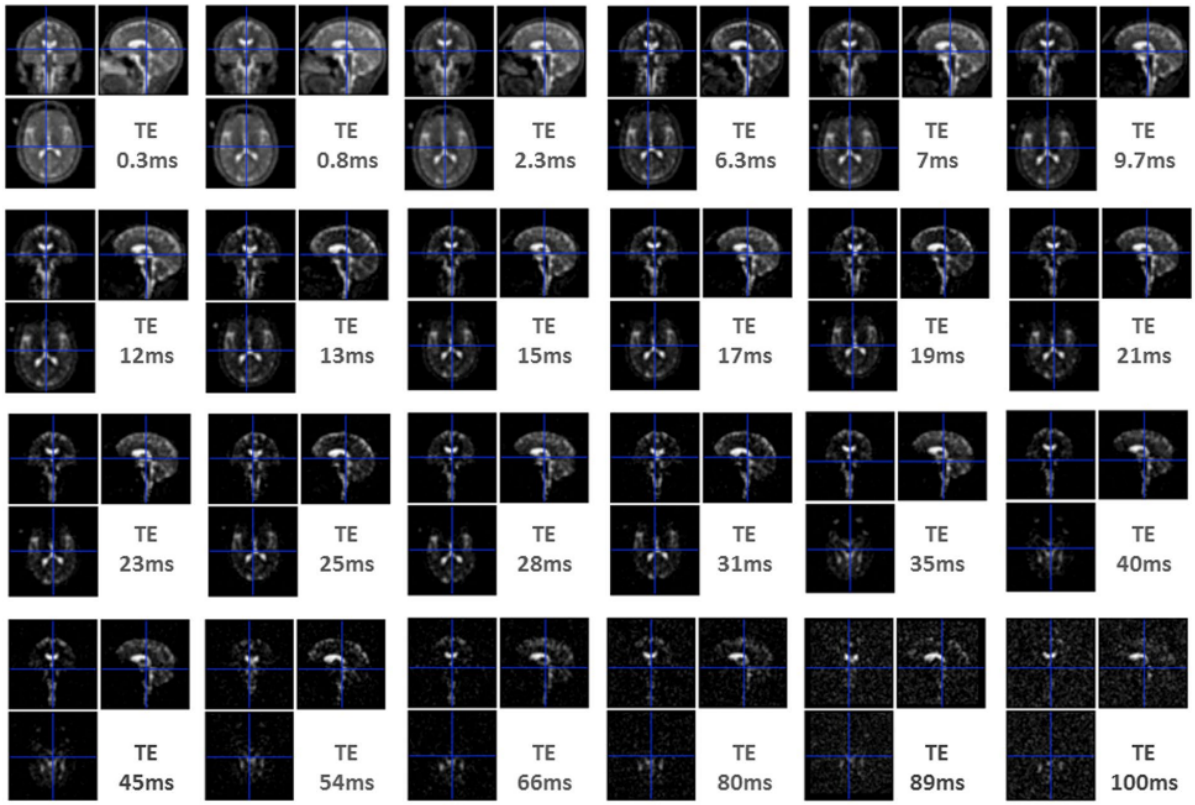

Figure 1.8: Example of multiple UTE acquisition on human brain at different echo times

projections have been acquired, Fourier transform can be used to obtain the image. So, UTE sequences allow to get the global shape of the image before the details.

Density-adapted 3D radial encoding using multi-echo UTE

Conventional multi-echo UTE acquisitions generally rely on uniformly sampled radial trajectories for k-space sampling. In these sequences, the sampling strategy does not take into account the distribution of signal energy across k-space, which may result in an inefficient use of acquisition time. Since the majority of image contrast and signal energy is concentrated near the center of k-space, uniform radial sampling can lead to unnecessary oversampling of high spatial frequencies while providing insufficient sampling on the central region.

To address this limitation, density-adapted 3D radial projection reconstruction [12], referred to as DARAD, modifies the sampling density along the radial trajectories. The central region of k-space is sampled more densely than the peripheral regions, where the signal contribution to the final image is lower. This strategy allows a more efficient allocation of sampling points while preserving the information that contributes most strongly to image quality and signal-to-noise ratio (SNR).

This approach is particularly relevant for sodium MRI, where the signal is intrinsically weak and rapidly decays. In radial acquisitions, the center of k-space is reached immediately after excitation, when the signal amplitude is at its maximum. As the readout progresses towards higher spatial frequencies, the signal progressively decreases due to T_2^* relaxation. By increasing the sampling density near the center of k-space, DARAD reconstruction places more sampling on the signal-rich portion of the acquisition while

reducing unnecessary sampling of peripheral regions where the signal has already substantially decayed.

Consequently, density-adapted radial encoding can improve acquisition efficiency and maintain image quality while potentially reducing the total acquisition time compared with conventional radial sampling strategies. These advantages make DARAD particularly well adapted for quantitative sodium MRI applications, where maximizing the intensity of the available signal is essential.

1.5 Challenges of quantitative ^{23}Na MRI

In MRI, image contrast is primarily qualitative, meaning that the signal intensity of a voxel depends on multiple factors such as nucleus density, relaxation properties and sequence parameters. As a result, signal intensities cannot generally be interpreted as direct measurements of a physical tissue property.

Quantitative mapping aims to overcome this limitation by estimating specific physical or biological parameters from MRI images and representing them as spatial maps. In a quantitative map, each voxel value corresponds to a measurable quantity with a defined physical meaning, allowing direct comparison between subjects, scanners, or acquisition protocols [13]. The generation of quantitative maps generally requires the acquisition of several images with varying sequence parameters and the fitting of a signal model to the measured data. The parameters obtained from this fitting procedure are then assigned to each voxel, providing maps of tissue properties such as relaxation times and tissue concentrations.

In sodium MRI, quantitative mapping is particularly relevant because it enables the estimation of sodium properties, related to tissue viability and ion homeostasis. Examples include total sodium concentration (TSC), longitudinal relaxation times and transverse relaxation times. These parameters may provide information that is not directly accessible through conventional qualitative imaging.

However, quantitative sodium mapping remains challenging due to the low SNR, the presence of multiple relaxation components, and the sensitivity of fitting procedures to noise and acquisition conditions. Then, dedicated acquisition strategies and robust parameter estimation methods are required to obtain reliable quantitative measurements.

1.5.1 Quantitative mapping

Beyond image acquisition, the extraction of quantitative biomarkers from sodium MRI data presents additional challenges. Quantitative mapping aims to estimate parameters such as sodium concentration, T_1 relaxation times and T_2^* relaxation times for which the measurements often require dedicated acquisition protocols and fitting signal models.

In the case of T_1 mapping, it can be performed using methods such as variable flip angle (VFA) acquisitions [14]. Nevertheless, few studies have investigated sodium T_1 relaxation mapping in the human brain at 7T. Only one relevant reference was identified in the literature: the work of Nagel et al. [15], which reported a mean whole-brain T_1 value of approximately 44.1 ms. In fact, major shares of the relaxation measurements in

sodium were done at 3T, and cannot be reliably translated to 7T to serve as reference values.

T_2^* mapping frequently relies on mono-exponential or bi-exponential fitting of multi-echo datasets [11]. However, these fitting procedures are highly sensitive to noise because several parameters must be estimated simultaneously from relatively low-SNR data. In particular, bi-exponential fitting may suffer from parameter coupling and non unique solutions, making the estimation of fast and slow relaxation components challenging. Consequently, well-defined acquisition protocol, appropriate fitting conditions and careful validation procedures are essential to obtain reliable quantitative sodium mapping.

In conclusion, the bi-exponential nature of sodium transverse relaxation represents a major challenge for quantitative mapping. The accurate characterization of relaxation components is particularly important for sodium MRI, since they may provide information about different tissue environments and micro-structures.

Several strategies have been proposed to compensate this limitation. The use of ultra-high magnetic field systems would increase the available magnetization and then improves the SNR. Optimized radial k-space trajectories, DARAD sequence and then advanced reconstruction techniques are generally used to maximize the intensity of the available signal.

1.6 Objectives of the Thesis

The main objective of this thesis is to assess the feasibility of generating quantitative sodium relaxation maps at 7T in phantoms and human brains and to evaluate their potentials for future applications in quantitative sodium imaging. In particular, the optimization of sodium image quality, parameter estimation and sequence acquisition choice (UTE and DARAD sequences) will be investigated in order to provide quantitative maps as good as possible.

Chapter 2

Materials and Methods

This chapter presents the different data and methods used during this thesis. It describes the processing pipeline applied to the sodium MR images. The acquisition protocol and pre-processing are explained as well. Then, T_1 and T_2^* estimation procedures are defined, as well as the optimization regarding the SNR. Each of these processing steps is described in detail in the following sections of this chapter.

2.1 Study materials

The data used in this work depends on the objective of each experiment. For T_1 estimation, a series of images acquired with different flip angles is required. In contrast, T_2^* estimation relies on a series of images acquired at different echo times. More details about these acquisition strategies are described in sections 2.3 and 2.4.

Both phantom and human data were used, but with different purposes. The main objective of this thesis is to generate quantitative maps of the human brain. However, phantom data are first used to test and optimize the acquisition sequences and their parameters, avoiding repeatedly scanning human subjects during the development phase. This is particularly important in ^{23}Na MRI, where acquisition times are significantly longer than in conventional ^{1}H MRI, making experiments more demanding for volunteers. Indeed, to obtain one set of multi-echo images for T_2^* estimation, 60 minutes are required to obtain 24 echos in ^{23}Na MRI [11], while 32 minutes only for ^{1}H similar procedure [16]. However, these acquisition times are highly dependent on the selected imaging sequence and acquisition parameters. The sodium acquisition protocol considered in [11] required 3 separate scans, each consisting of 8 echoes, resulting in a total scan duration that may not be practically achievable within the constraints of this study.

For these reasons, the sequences were first optimized on phantoms under controlled conditions, and then applied to human data once satisfactory performance is achieved.

2.1.1 Phantom data

Two phantoms were used in this study. Both are filled with a different solution of water, agar and sodium, allowing them to produce a detectable signal in sodium MRI. The first phantom used was spherical and was designed as phantom 1, while the second one was cylindrical and was designed as phantom 2.

It is important to note that many types of phantoms can be designed for sodium MRI experiments. Here, only phantoms filled of liquid gel were used for simplicity. However, more complex phantoms can be constructed, for example using denser agarose gel or multiple compartments with different sodium concentrations and physical properties. Liquid gel phantoms mainly represent free sodium ions, similar to those found in CSF or in the extracellular space. These environments are characterized by relatively unrestricted motion and longer relaxation times. In contrast, dense agarose-based phantoms better mimic biological tissues because high concentration of agarose should induce more restricted motion of sodium atoms, leading to shorter relaxation times. This one is closer to the intracellular environment and structured tissues, but human brain are still needed in order to estimate the impact of the intra- and extracellular components, which can not be represented by a simple phantom.

Ideally, a realistic phantom would combine both free and restricted sodium compartments. However, for practical reasons, only gel sodium phantoms were used in this work.

2.1.2 Human brain data

Despite the more complex structure and the difficulty to reach good image quality, human data are essential to evaluate the performance of the proposed methods in realistic conditions. They allow to determine the ability of the sequences to capture important physiological information and, then, to generate coherent quantitative T_1 and T_2^* maps *in vivo*.

The brain data used for this work were acquired on volunteers that have signed a written informed consent to participate in the study, which was approved by the local ethical committee.

2.2 Sequence parameter optimization for SNR improvement

The signal generated by ^{23}Na nuclei in MRI is known to be much lower than the one of ^{1}H nuclei. As a consequence, the resulting SNR is decreased and leads to more difficult data processing. Improving the SNR is then critical when the signal is as low as the one of ^{23}Na MRI and this section explain the SNR maximization via the optimization of the sequence parameters, including excitation flip angle, repetition time, and the number of projections in k-space (N_p).

The optimization of these parameters is essential to reach good sodium image quality within clinically acceptable scan durations. In conventional ^{1}H MRI, optimization of these parameters relies on the Ernst angle method [17]. However, it does not account for practical acquisition limitations such as specific absorption rate (SAR) restrictions and total acquisition time (TA). Since parameters that generally improve SNR often come with longer scan durations or higher RF energy deposition, a trade-off is considered: increasing the number of projections improves the SNR, but also increases the acquisition time or the SAR value.

To optimize the SNR, the signal intensity of a spoiled gradient echo acquisition will be used. It depends on the repetition time (TR), flip angle (FA), and T_1 and according

to [18]. Then, the MR signal (S) in the steady-state is proportional to:

$$S \propto \frac{\sin(\mathrm{FA})\left(1 - e^{-\mathrm{TR}/T_1}\right)}{1 - \cos(\mathrm{FA})e^{-\mathrm{TR}/T_1}} \tag{2.1}$$

For radial acquisitions such as density-adapted radial acquisition (DARAD), the SNR will also depend on the number of encoding steps, which in this case corresponds to the number of projections in k-space N_p. Then, the SNR can be approximated by the product of the signal intensity and the square root of the number of radial projections, and can be approximate by:

$$\mathrm{SNR} \propto S\sqrt{N_p} \tag{2.2}$$

However, equation 2.2 includes multiple interdependent parameters, rendering multi-parametric optimization difficult due to the possibility to reach local extremum. In fact, as several combinations of parameters could lead to similar results, some local combinations can influence the convergence of solutions through local optimization maxima.

To address this problem, constraints can be introducing in order to reduce the number of free parameters. The first constraint will link the total acquisition time, the number of projections and the repetition time in order to keep the scan duration constant:

$$\mathrm{TA} = N_p.\mathrm{TR} \tag{2.3}$$

The second constraint will set the SAR value. The SAR represents the amount of RF energy absorbed in tissue and must not exceed safety limits in order to prevent excessive tissue heating (see section 1.4.1). Fixing the SAR ensures that the acquisition remains within safety limits while allowing a relationship between flip angle and repetition time to be established. In addition, based on one of the works of Novikov and al.[18], the specific absorption rate, depending on flip angle and repetition time, can be approximated as:

$$\mathrm{SAR} \propto \frac{\mathrm{FA}^2}{\mathrm{TR}} \tag{2.4}$$

These two constraints illustrated in equations 2.3 and 2.4 are interesting because their do not affect noise in the MR signal S. The noise can then be assumed to be constant while varying the flip angle, repetition time and number of projections in the sequence.
To verify these relationship, phantom acquisitions will be used in order to confirmed this dependence (see section 2.2.1).

Using fixed values of acquisition time and SAR, both the flip angle and the number of projections can be expressed as functions of TR. Consequently, the equations 2.3 and 2.4 can be rewritten:

$$\mathrm{FA} \propto \sqrt{\mathrm{SAR} \cdot \mathrm{TR}} \tag{2.5}$$

$$N_p = \frac{\mathrm{TA}}{\mathrm{TR}} \tag{2.6}$$

This allows the SNR equation 2.2 to be expressed as a function of a single variable, TR, ensuring that acquisition parameters remain within safe limits in keeping constant scan duration.

The SNR equation 2.2 can finally be expressed as:

$$\mathrm{SNR}(\mathrm{TR}) \propto \frac{\sin\left(\sqrt{\mathrm{SAR}\cdot\mathrm{TR}}\right)\left(1-e^{-\mathrm{TR}/T_1}\right)}{1-\cos\left(\sqrt{\mathrm{SAR}\cdot\mathrm{TR}}\right)e^{-\mathrm{TR}/T_1}}\sqrt{\frac{\mathrm{TA}}{\mathrm{TR}}} \tag{2.7}$$

In this relationship, the SAR, TA and T_1 are fixed, so that the optimization can be done only on TR. Then, equation 2.7 removes the need to perform multi-parametric optimization, alleviating the possibility of convergence to local extrema, and allowing to find globally optimal SNR within the defined constraints.

2.2.1 Optimization procedure and data acquisition

Experimental validations of equations 2.2 and 2.4 were performed on a 7T Terra MRI (Siemens Healthineers, Erlangen, Germany) scanner using a dual-tuned ^{1}H /^{23}Na birdcage head coil (RAPID Biomedical, Rimpar, Germany). The homogeneous sodium phantom 1 with a measured T_1 relaxation time of approximately 50 ms was used for all experiments. The acquisitions were performed using a density-adapted 3D radial (DARAD) sodium MRI sequence. This sequence was preferred to the classic UTE sequence because the paper presented by Novikov and al. [18] shows that density-adapted radial sequence has better SNR.

Three acquisition series were performed to validate the theoretical relationships related to the constraints applied for the SNR optimization. The initial parameters were: field of view = 220 mm^3, voxel size = 3.93 mm^3 and TA = 6:13 min.

First, phantom acquisitions were performed with varying repetition times to investigate the relationship between the time-averaged SAR and TR. The repetition time was varied between 10 and 45 ms (TR = 10, 15, 20, 25, 30, 35, and 45 ms), while the flip angle, number of projections, and echo time were kept constant (FA = 10°, N_p = 2000, TE = 0.15 ms).

Next, acquisitions with different flip angles were carried out to assess the dependence of time-averaged SAR on FA. In this case, the flip angle ranged from 6 to 37° (FA = 6, 12, 25, and 37°), while the remaining acquisition parameters were fixed (TR = 12.8 ms, TE = 0.27 ms, N_p = 20000).

Finally, datasets reconstructed with different numbers of radial projections were analyzed to evaluate the expected dependence of SNR on $\sqrt{N_p}$. The number of projections was varied from 2000 to 32000 (N_p = 2000, 4000, 8000, 16000, and 32000), while TR, TE, and FA were kept constant (TR = 25 ms, TE = 0.1 ms, and FA = 22°).

The constrained SNR optimization of equation 2.7 was performed numerically using the `Minimize` function from SciPy optimize v1.17.0 library. The acquisition time was fixed to 6 min and 13 sec and the SAR was constrained to the IEC safety limit for head imaging at 7T, corresponding to 3.2 W/kg [9]. The optimal TR was then derived from equation 2.7 and the corresponding flip angle satisfying the SAR constraint was calculated via equation 2.5. The number of projections was then determined from the acquisition time constraint 2.6. It gives the optimal set of parameters including the repetition time, the flip angle and the number of projections that maximizes the constrained SNR.

After validation of the theoretical model, an acquisition on phantom 1 was performed using the optimized TR, flip angle and number of radial projections and this was then compared with four TR sub-optimal acquisitions acquired under the same acquisition

time and SAR constraints. All the parameters used during this optimization validation are summarized in Table 2.1, using TE set at 0.15 ms.

Data	**TR (ms)**	**FA (°)**	N_p
Optimized data			
	25	38	14722
Sub-optimized data			
Scan 1	5	17	73600
Scan 2	50	53	7396
Scan 3	100	76	3684
Scan 4	140	90	2632

Table 2.1: Acquisition parameters of the phantom 1 images used for the SNR optimization

2.2.2 SNR comparison

The SNR was computed according to the smoothed image subtraction (SIS) method described in this article [19]. The SIS method estimates noise by subtracting a smoothed version of the image to the original image, resulting in a residual image. The smoothing operation was done using an uniform filter width of 4 pixels and preserves the global signal content, while the residual image is assumed to mainly contain random noise.

The signal for the SNR computation is then calculated as the mean pixel value (MPV) in the raw image, and the noise value as the standard deviation of PV from the residual image.

$$\mathrm{SNR} = \frac{\mathrm{MPV}}{\mathrm{SD}_{\mathrm{residual}}} \tag{2.8}$$

where MPV is extracted from the original image, $\mathrm{SD}_{\mathrm{residual}}$ is the standard deviation in the residual image obtained from the original image after the subtraction of the smoothed one. Figure 2.1 illustrates the different steps of the SIS method.

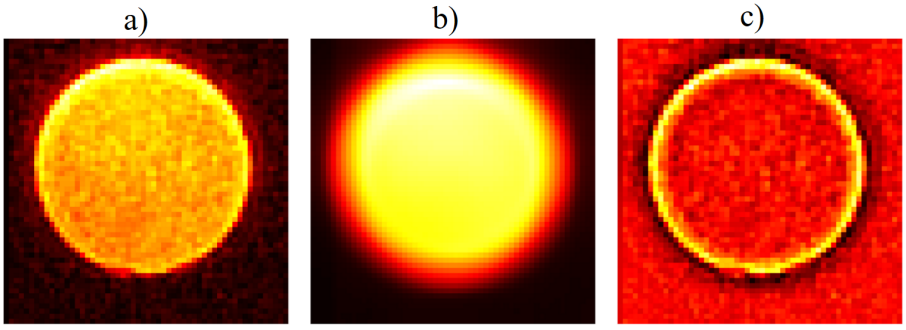

Figure 2.1: SIS method example using the phantom 1: a) raw image, b) smoothed image using an uniform filter and c) residual image obtained from the subtraction of the smoothed image to the original one

2.3 T1 estimation

The variable flip angle (VFA) method [14, 17] is widely used in both ^{1}H and ^{23}Na MRI to rapidly estimate T_1 relaxation times over a full 3D volume. This approach is particularly suitable when acquisition time must be kept short in the context of medical routine. The VFA method relies on acquiring multiple spoiled gradient echo images at different flip angles, while keeping other acquisition parameters constant. The resulting signal variation as a function of the flip angle is then fitted voxel-wise to estimate the T_1 relaxation time.

Under steady-state conditions, the transverse magnetization immediately after RF excitation can be written as:

$$M_{xy}(\mathrm{FA}) = M_0 \frac{1 - e^{-\mathrm{TR}/T_1}}{1 - \cos(\mathrm{FA}) e^{-\mathrm{TR}/T_1}} \sin(\mathrm{FA}) \tag{2.9}$$

where M_{xy} is the transverse magnetization, M_0 is the equilibrium magnetization, TR is the repetition time, and T_1 is the longitudinal relaxation time. Equation 2.9 is obtained by solving the Bloch equations in steady-state conditions. Figure 2.2 illustrates the dependence given by the equation 2.9 for a given set of parameters.

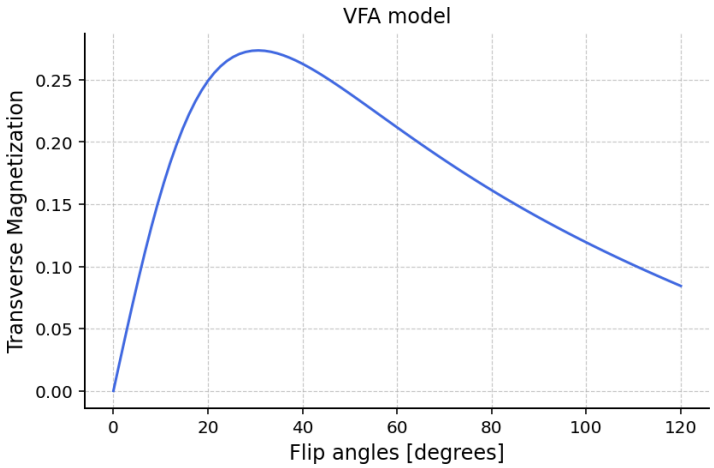

Figure 2.2: Variable flip angle model using $M_0 = 1$, $T_1 = 100$ and TR = 15

The measured signal intensity is proportional to transverse magnetization and can be expressed as:

$$S \propto \frac{1 - e^{-\mathrm{TR}/T_1}}{1 - \cos(\mathrm{FA}) e^{-\mathrm{TR}/T_1}} \sin(\mathrm{FA})\, e^{-\mathrm{TE}/T_2^*} \tag{2.10}$$

where TE is the echo time and T_2^* is the effective transverse relaxation time, using a mono-exponential transverse magnetization decay approximation.

To generate a quantitative T_1 relaxation map, several images were acquired in the steady-state conditions described by equation 2.10 using different flip angles. The flip angle is a sequence parameter that determines the rotation of the net magnetization away from its equilibrium in the longitudinal direction (see section 1.4.2). By varying the flip

angle, it is possible to sample the dependence of the signal on FA and estimate the T_1 value using an appropriate signal model.

It is important to note that the flip angle in ^{23}Na MRI used in VFA method are generally lower than those employed in conventional ^{1}H MRI under similar acquisition conditions. Even if larger flip angles may improve the precision of T_1 estimation and increase signal intensity when approaching the Ernst angle, their use is limited by SAR constraints and practical acquisition time considerations. Consequently, smaller flip angles are often preferred in sodium MRI to achieve a balance between SAR, SNR, and scan duration.

2.3.1 Data acquisition

The images used to generate T_1 relaxation maps were acquired using two sequences: UTE and DARAD with similar parameters in phantom while only DARAD sequence was used for volunteers. In fact, the UTE sequence was not used for human imaging because of its lower SNR compared to the one obtained using the DARAD sequence [18]. The acquisitions were performed on a 7T Terra MRI (Siemens Healthineers, Erlangen, Germany) scanner using a dual-tuned ^{1}H /^{23}Na birdcage head coil (RAPID Biomedical, Rimpar, Germany). All the relevant parameters used for the T_1 estimation are regrouped in Table 2.2.

Parameter	**Phantom 2**	**Human**
Sequences	UTE and DARAD	DARAD
TR (ms)	17	17
TE (ms)	0.15	0.15
Number of projections	21947	21947
FA (°)	30, 26, 22, 18, 14	30, 25, 20, 10
TA (minutes)	6:13	6:13
Field of view	220	220
Voxel size (mm^3)	3.93	3.93
Pulse duration (µs)	230	230

Table 2.2: Acquisition parameters for T_1 estimation for phantom 2 and human scans

2.3.2 Pre-processing

The acquired data were first realigned with respect to the first echo acquired at the lowest TE using the SMP12 [20] function `realign:Estimate and Reslice` in MATLAB, allowing all images used for the fitting procedure to be recentered. This step is particularly important in human imaging, as it reduces the effects of motion between acquisitions performed at different flip angles. In contrast, it can be omitted when working with static phantoms, where no motion is expected. Misalignment may result from different types of patient motion, including head or body movements, breathing, or coughing. In the

context of this thesis, motion correction is essential to ensure that the voxel grid remains spatially consistent if the data is acquired in several scans, so that each voxel corresponds to the same tissue location from one acquisition to another.

In sodium MRI, denoising is an important pre-processing step. Applying denoising helps improve the robustness of subsequent processing steps such as brain extraction and segmentation. However, the choice of denoising method must be made carefully, since excessive filtering may attenuate or remove relevant anatomical details. In this work, the LCPCA denoising from hMRI SPM12 toolbox was used [21].

This project focuses on the analysis of brain images and phantoms only. For human brain data, masking was performed using the SPM12 segmentation tool, where the white matter, gray matter and CSF probability maps were created. Then, a Python script generated the brain mask from the probability maps in the form of a boolean map. The maps were binarized and combined using a voxel-wise logical operation to create a single brain mask, where each voxel belonging to at least one of the three tissue probability maps was accepted. For phantom images, a dedicated Python script was developed to retain only the geometric shape corresponding to the phantom based on a percentile threshold. The image was first smoothed with a gaussian filter to reduce noise, then thresholding was applied to separate the phantom from he background. The largest connected component was finally retained and inner holes were filled, resulting in the final binary mask.

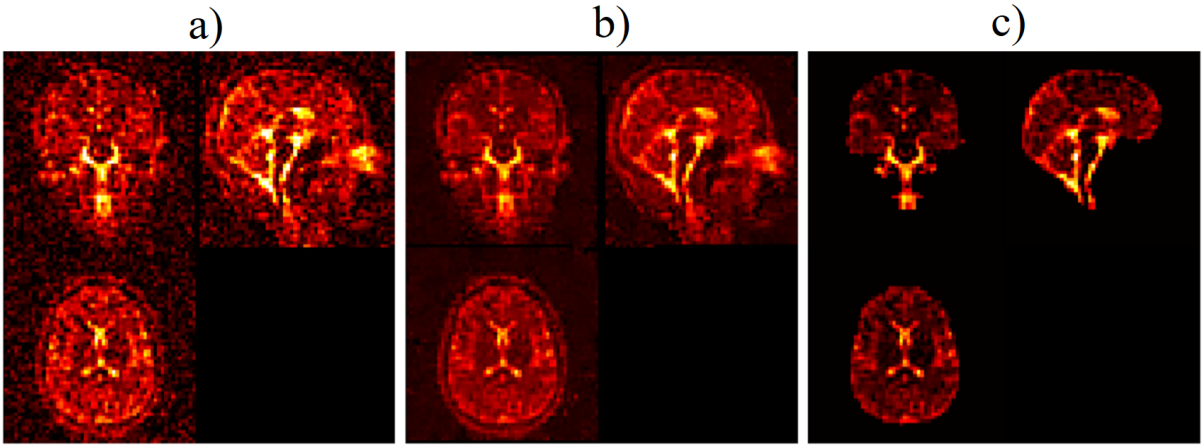

Figure 2.3: Human brain pre-processing steps: a) unprocessed image, b) image after realignment and denoising, c) masked image.

These pre-processing steps are illustrated in Figure 2.3 and provide a consistent set of images ready for the subsequent fitting procedure used to generate quantitative relaxation maps. The same pipeline was applied to all datasets.

2.3.3 R^2-map comparison

Evaluating the goodness of fit is a crucial step in the evaluation of the VFA model. It is important to verify that the estimated parameters accurately describe the measured data. A poor fit may lead to unreliable parameter maps and misinterpretation of the underlying tissue properties.

One common metric used to evaluate the quality of the fit is the coefficient of determination, denoted as R^2. For each voxel, the R^2 value quantifies how well the fitted model reproduces the experimental signal evolution. Values close to 1 indicate an excellent agreement between the model and the measured data, whereas lower values suggest a less accurate fit. By computing the R^2 value voxel-wise across the entire image, an R^2-map can be generated. This map gives a spatial representation of the fitting quality and can be taken into account for the interpretation of the corresponding T_1 maps.

To compare the fitting performance obtained with different methods or sequences, the distribution of the R^2 values will analyzed. A simple and effective approach consists in plotting the histograms of the different R^2 maps on the same graph. It leads to a visual comparison allowing the evaluation of both the fitting quality and the spread of the R^2 values. A distribution shifted towards higher R^2 values generally indicates a more robust and accurate fitting procedure.

2.3.4 Data processing

After the pre-processing, the images are used to generate the T_1 relaxation map. The equation 2.9 is then fitted using the global optimization `dual annealing` from the Python library `scipy.optimize` [22] in order to find the global maximum of the function, avoiding falling into local maximum. The acquired data were fitted voxel-wise according to the equation 2.9, using the known TR and flip angle values from the acquisition protocol. The parameters M_0 and T_1 were estimated by minimizing the difference between the measured signal and the VFA model via the Mean Squared Error (MSE) method.

The results consist three different maps: a T_1-map, a S_0-map corresponding to the value of M_0 and an R^2-map, representing the accuracy of the fitting method.

2.4 T_2^* estimation

The aim of this part is to generate quantitative T_2^* relaxation maps for both phantom and human brain data. In contrast to T_1 mapping, which relies on varying the flip angle, T_2^* estimation is based on acquiring a series of images at different echo times. By sampling the signal decay over time, it is possible to estimate the transverse relaxation properties of sodium.

2.4.1 Theory

T_2^* relaxation reflects both intrinsic tissue properties, represented by T_2, and additional dephasing effects caused by magnetic field inhomogeneities (see section 1.4.4). In sodium MRI, T_2^* decay is particularly fast and often results in a multi-component behavior because ^{23}Na ions exhibit different types of motion, leading to the presence of two different sodium populations. It means that the measured signal is the sum of multiple decays, it can then be difficult to estimate and separate these two T_2^* components. Two models were used to illustrate the transverse relaxation values for the two populations of sodium: mono-exponential and bi-exponential decay models.

Mono-exponential model

A first approximation consists in modeling the signal decay using a mono-exponential function. It represents the signal decay over time and is determined by the equation 2.11.

$$S(t) = S_0\, e^{-t/T_2^*} \tag{2.11}$$

where S_0 is the initial transverse magnetization just after the RF pulse application, t is the time and T_2^* is the effective transverse relaxation time.

This model is simple and robust but it assumes a single exponential decaying signal, which is not realistic for human sodium imaging, excepted for liquid like structures, such as CSF. This method is in general the one used for uniform phantoms, and in human in first time even if it is not representative of the MRI physics of human brain. To properly model the brain properties, the bi-exponential model would be preferred because of its better modeling of human tissues.

Bi-exponential model

In biological tissues, sodium is distributed across different compartments, mainly intracellular and extracellular spaces, which exhibit different relaxation behaviors (see section 1.4.4). As said before, it leads to a multi-exponential signal decay and a more accurate model is therefore given by a bi-exponential function:

$$S(t) = S_0(f e^{-t/T_{2,\mathtt{fast}}^*} + (1-f)\, e^{-t/T_{2,\mathtt{slow}}^*}) \tag{2.12}$$

where S_0 is the initial transverse magnetization just after the RF pulse application, f is the signal fraction of the fast transverse relaxation time, t is the time, $T_{2,\mathtt{fast}}^*$ and $T_{2,\mathtt{slow}}^*$ are the fast and the slow relaxation times, respectively.

This model provides more detailed information about tissue microstructure, but requires higher SNR and more echo samples to ensure stable fitting compared to mono-exponential model. The Figure 2.4 illustrates the two models of exponential decay using realistic parameters for both models. The bi-exponential model has a faster decay compared to the mono-exponential model, which is expected regarding the physic properties of sodium imaging.

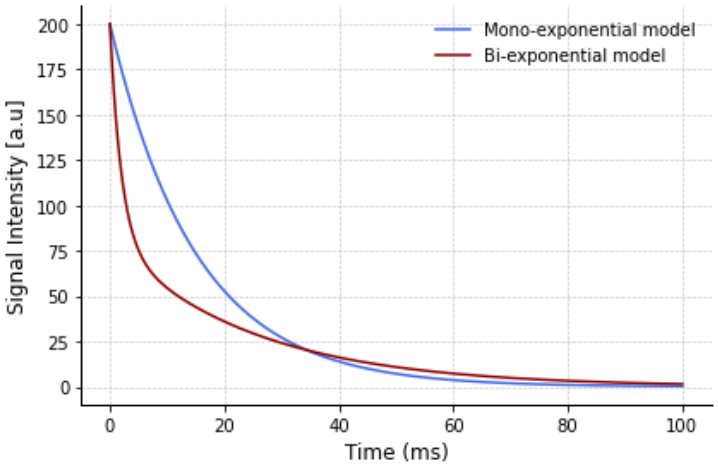

Figure 2.4: Mono-exponential ($S_0 = 200$, $T_2^* = 15$ ms) and bi-exponential ($S_0 = 1500$, $f = 0.6$, $T_{2,\mathtt{fast}}^* = 2$ ms, $T_{2,\mathtt{slow}}^* = 25$ ms) decays in ^{23}Na MRI.

Rician noise model

Noise plays a critical role in all low SNR applications in quantitative imaging and must be properly considered during signal modelling, especially in ^{23}Na MRI. In the case of this thesis, magnitude MRI data was acquired, which has noise that follows a Rician distribution. This introduces a positive bias in the measured signal, particularly in low SNR conditions.

In the context of multi-echo sodium MRI, Ridley et al. [11] highlighted the importance of accounting for Rician noise when estimating relaxation parameters and sodium concentrations. The sodium signal is modeled using a bi-exponential decay reflecting short and long T_2^* components. When magnitude images are used, the measured signal can be approximated as:

$$S(t) = \sqrt{S_0^2 \left(f e^{-t/T_{2,\mathtt{fast}}^*} + (1-f)\, e^{-t/T_{2,\mathtt{slow}}^*} \right)^2 + \sigma_{\mathtt{rician}}^2} \tag{2.13}$$

where $\sigma_{\mathtt{rician}}$ represents the Rician noise amplitude parameter.

Accounting for Rician noise is essential for improving the accuracy of quantitative sodium MRI, especially when estimating short T_2^* components using low-intensity signals. Ignoring this effect may lead to biased relaxation time estimations and inaccurate sodium concentration measurements.

It is important to note that the method used in this work to evaluate the noise does estimate it as gaussian [19]. In fact, the SIS method introduced in section 2.2.2 does not consider the noise as rician because it computes the $\mathrm{SD}_{\mathrm{residuals}}$ as gaussian noise. That is why we had to add a factor of correction to go from the gaussian noise to the Rician noise in order to be able to use it correctly into the equation 2.13. Then, the Gaussian noise estimated by the SIS method can be adapted by multiplying it by the Rayleigh factor:

$$\sigma_{\mathtt{rician}} = \sigma_{\mathtt{gauss}} \sqrt{\frac{\pi}{2}} \tag{2.14}$$

This equation is an approximation of the real noise in sodium MR images. The real noise is nevertheless different but the approximation given by equations 2.13 and 2.14 are sufficient for the relaxation parameter estimation.

Optimization of the echo selection

The selection of the echo times is an important parameter for signal acquisition affecting the precision of relaxation curve parameter estimation. Both the number of echoes and their temporal distribution can strongly influence the characterization of the signal decay as well as the total acquisition time. Choosing more echos densely and uniformly spread from 0 to 5 times the expected long T_2^* component would be best for the fitting precision, but this approach presents one main problem.

The first acquisition was performed using 12 echos from 0.1 to 10.5 ms. However, according to the work of Qian et al. [23], only 8 echoes will be used to model the free induction decay. Indeed, reducing the number of echoes shortens the acquisition time, which is beneficial for patient comfort and clinical feasibility.

Limiting the acquisition to 10.5 ms may segment part of the exponential decay. As illustrated in Figure 2.4, the signal may still be decaying after this time point. This

particularly affects the estimation of the slow T_2^* component, since it mainly contributes to the later part of the FID. Consequently, an insufficient echo range may lead to biased estimates of the slow relaxation component. To investigate the influence of the echo range on parameter estimation, simulated phantoms were generated and analyzed using different TE ranges.

Simulated phantoms

Simulated phantoms provide a flexible tool for evaluating fitting methods without requiring MRI scanner time or patient acquisition. It makes it possible to test different parameter configurations and processing strategies under controlled conditions, particularly for evaluating the quality of fit or the impact of the selected echo range, as discussed in the previous section.

Simulated datasets were generated using predefined parameter values. For the mono-exponential model, the simulations included T_2^* and S_0 as exposed in equation 2.11. For the bi-exponential model, the simulations included $T^*_{2,\texttt{fast}}$, $T^*_{2,\texttt{slow}}$, S_0, and the fast signal fraction f, according to the equation 2.12. Two types of phantoms were simulated: homogeneous phantom and heterogeneous phantom composed of two regions with distinct relaxation properties.

In the case of homogeneous phantoms, identical parameter values were assigned across the entire phantom volume. Then, the signal evolution was simulated using 8 different echo times, each corresponding to a different range of echo times. Rician noise as considered in equation 2.14 was then added to the images by introducing Gaussian-distributed noise into the image before taking the absolute value of the whole image. The noise level $\sigma_{\texttt{gauss}}$ was ideally selected to produce similar SNR to those observed in experimental sodium MRI data. However, although this remains an approximation, it provides a realistic framework for evaluating the fitting procedures, but it should be used with care. Indeed, the statement of this noise can not be correctly measured in an exact way via experiments.

2.4.2 Data acquisition

In this section, simulated phantoms generation through artificial procedures and the data acquisition related to phantoms and human brain are described.

Phantoms and human brain acquisition

The data used to estimate T_2^* components in phantom 2 and human brain were acquired using both UTE and DARAD sequences. As exposed in 2.3, only DARAD sequence was use for volunteers. The images were acquired with similar 7T Terra MRI machine than in section 2.3.1 and the relative sequence parameters are summarized in Table 2.3.

Simulated phantom experiments

Simulated phantoms were used to evaluate the fitting procedures under controlled conditions without requiring experimental MRI acquisitions. The size of phantom was set at 16x16x16 pixels in a total image size of 20x20x20 pixels.

First, two TE ranges were compared: a short range extending from 0.15 to 10.5 ms (0.15, 0.2, 0.35, 1.5, 5.42, 7.5, 9 and 10.5 ms), and a longer range extending from 0.15 to

Parameter	**Phantom 2**	**Human**
Sequences	UTE and DARAD	DARAD
TR (ms)	200	200
TE (ms)	0.15, 0.35, 1, 5, 15, 35, 60, 80	0.15, 0.35, 1, 5, 15, 35, 60, 80
Number of projections	1865	1865
FA (°)	90	90
TA (minutes)	6:13	6:13
Field of view (mm^3)	220	220
Voxel size (mm^3)	3.93	3.93
Pulse duration (µs)	230	230

Table 2.3: Acquisition parameters for T_2^* estimation for phantom 2 and human scans

80 ms (0.15, 0.35, 1, 5, 10, 35, 60 and 80 ms), both using mono- and bi-exponential decay models with ($T_2^* = 20$ ms and $S_0 = 200$) and ($T_{2,\texttt{fast}}^* = 3$ ms, $T_{2,\texttt{slow}}^* = 25$ ms, $S_0 = 200$, $f = 0.6$ and $\sigma_{\texttt{gauss}} = 3$), respectively.

Second, the impact of noise level was investigated. Three simulations using the long echo time range of 80 ms with 8 echos was generated for mono- and bi-exponential models using the same model parameters than for the echo range comparison. Each of then includes a different level of noise in function of the chosen model.

For the mono-exponential model, $\sigma_{\texttt{gauss}} = 3$, 30 and 60 were tested, corresponding to an approximate SNR of 66, 7 and 3, respectively. The value $\sigma_{\texttt{gauss}} = 30$ was selected for mono-exponential model because it approximately reproduces the SNR measured in real phantom acquisitions.

However, due to the increased complexity and instability of the bi-exponential fitting procedure, lower noise levels were required to obtain meaningful parameter estimations. Simulations were therefore carried out using $\sigma_{\texttt{gauss}} = 1$, 3, and 10 in order to artificially increase the SNR. It leads to an approximate SNR of 195, 66 and 20, respectively. Although these noise levels are lower than those found in realistic sodium MRI acquisitions, they remain useful for evaluating the intrinsic sensitivity of the bi-exponential model to noise.

Third, the accuracy of parameter estimations was determined using two different types of simulated phantoms, one homogeneous and the other heterogeneous, as exposed in the previous section. Mono- and bi-exponential T_2^* estimations were performed on datasets using the parameters summarized in Table 2.4, where the values are consistent with relaxation properties reported in the literature [11, 15].

Finally, simulated phantom data were generated using a bi-exponential signal model with the following parameters: $T_{2,\texttt{fast}}^* = 3$ ms, $T_{2,\texttt{slow}}^* = 25$ ms, $S_0 = 200$, $f = 0.6$ and $\sigma_{\texttt{gauss}} = 3$. Both mono-exponential and bi-exponential fitting procedures were then applied to the same simulated dataset. These results will be used to evaluate the error

	S_0	T_2^* (ms)	$T_{2,\texttt{fast}}^*$ (ms)	$T_{2,\texttt{slow}}^*$ (ms)	f	$\sigma_{\texttt{gauss}}$
Mono-exponential						
Homogeneous	200	20	–	–	–	30
Heterogeneous	200	15	–	–	–	30
	300	25	–	–	–	30
Bi-exponential						
Homogeneous	200	–	3	35	0.6	3
Heterogeneous	200	–	2	30	0.5	3
	300	–	4	20	0.7	3

Table 2.4: Parameters used for the simulated phantom accuracy experiments.

done using the mono-exponential fitting while a bi-exponential decay is expected.

2.4.3 Pre-processing

The pre-processing for the data used to generate T_2^* quantitative maps is similar to the one used in the previous section 2.3. The segmentation procedure was modified for human brain data, separate masks of the CSF and the combination of white and gray matter were done instead of whole-brain segmentation used for T_1 calculation, still using the SPM12 segmentation tool. It was necessary in this case because the relaxation properties of sodium ions are different: the CSF is considered as having a mono-exponential decay behavior, and the rest of the tissues has bi-exponential decay. The segmentation is then mandatory to separate the two compartments.

2.4.4 Data processing

Following the pre-processing steps, the different echo images were used to generate quantitative T_2^* relaxation maps. For phantom 1, the mono-exponential model described by Equation 2.11 was fitted voxel-wise across the echo images using the `dual_annealing` global optimization algorithm, following a procedure similar to that described in Section 2.3. The parameters S_0 and T_2^* were also estimated by minimizing the MSE between the measured signal and the model prediction.

The fitting procedure applied to the simulated phantom data was identical to the one used for the experimental phantom acquisitions.

For the human brain data, two fitting approaches were investigated. First, a mono-exponential model (equation 2.11) was applied voxel-wise to the whole brain. Second, a bi-exponential model (equation 2.12) was fitted to the white matter and gray matter regions, while the mono-exponential model was retained for the CSF. As for the phantom data, all model parameters were estimated voxel-wise using global optimization.

For the mono-exponential model, three quantitative maps were generated: a T_2^*-map, an S_0-map, and an R^2-map. For the bi-exponential model, five maps were obtained: a $T_{2,\texttt{fast}}^*$-map, a $T_{2,\texttt{slow}}^*$-map, a signal fraction map, an S_0-map, and an R^2-map.

To assess the quality and plausibility of the fitted parameters, histograms of the estimated parameters and R^2 values were generated. These histograms represent the distribution of the fitted parameter values across all voxels inside the corresponding mask. The location and spread of the distributions provide information about the consistency of the fitting procedure, where the presence of outliers or multiple peaks may indicate fitting instabilities or tissue heterogeneity. In addition, the R^2 distributions were used to evaluate the goodness of fit of the different relaxation models. The resulting parameter distributions were compared with values reported in the literature.

2.5 Code availability

All the codes used in this work are available on the ULiège GitLab repository[1]. These scripts were developed for research purposes and are provided in their current form. They have not been fully optimized and include comments and intermediate processing steps.

[1] https://gitlab.uliege.be/CyclotronResearchCentre/Methods/23na_mri/t2star-fitting-and-preprocessing

Chapter 3

Results

This chapter presents the results obtained using the methodologies described in Chapter 2. The analyses include simulated phantom experiments, SNR optimization, T_1 mapping, and T_2^* estimation using both mono-exponential and bi-exponential fitting approaches.

3.1 Simulated phantom results

Mono- and bi-exponential T_2^* estimations were performed on datasets generated with predefined parameters and controlled noise levels. The fitting was applied voxel-wise in the same way as for real acquisitions. The estimated parameters were subsequently represented using histograms in order to assess the robustness and precision of the different fitting approaches across the entire phantom volume.

3.1.1 Echo range comparison

As discussed in the previous chapter, the selected echo time range directly influences the estimation of the relaxation parameters and signal amplitude. Two TE ranges were therefore compared: a short range extending from 0.15 to 10.5 ms and a longer range extending from 0.15 to 80 ms. The corresponding parameter distributions obtained with the mono- and bi-exponential models are presented in Figures 3.1 and 3.3, respectively.

Mono-exponential model

The mono-exponential estimated parameters are illustrated in Figure 3.1 for the two TE ranges. The shorter echo range leads to a slightly narrower distribution around the expected T_2^* value, which could initially suggest a more precise estimation. However, the corresponding R^2 distributions shown in Figure 3.2 demonstrate that the overall fitting quality is substantially better when the 80 ms range is used. For the shortest TE range, several negative R^2 values are even observed, indicating that the fitting procedure performs worse than a simple mean-value approximation of the signal. This apparent contradiction could be explained by the incomplete sampling of the signal decay when only short echo times are acquired. Since the acquisition stops early, the fitting mainly captures the initial part of the decay curve and becomes less sensitive to deviations occurring at longer echo times. Consequently, the fitted parameters may appear more concentrated while still failing to accurately represent the full signal evolution. Extending the TE range to 80 ms provides a more complete description of the decay behavior and therefore improves the global fitting performance.

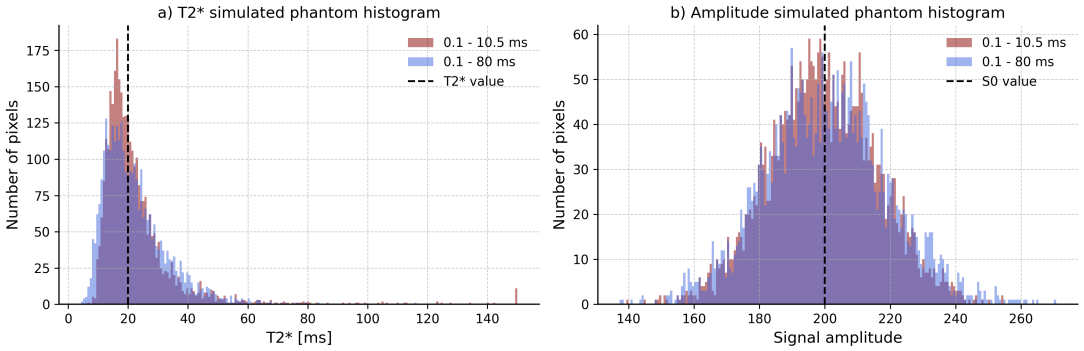

Figure 3.1: Parameter distributions obtained with the mono-exponential model using different echo ranges for the simulated phantom.

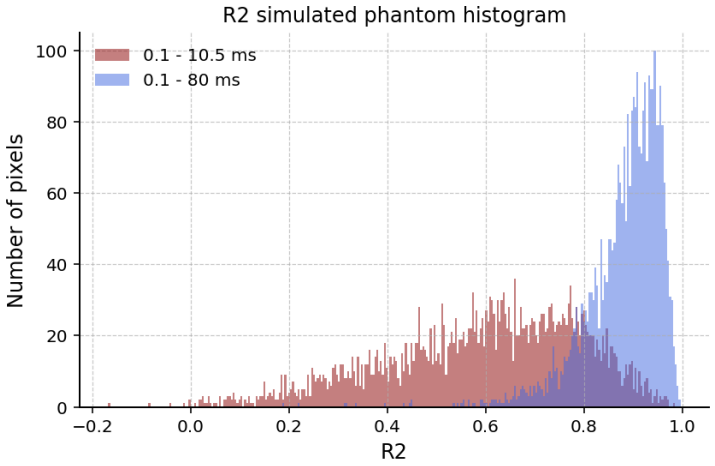

Figure 3.2: R^2 distributions obtained with the mono-exponential model using different echo ranges for the simulated phantom.

Bi-exponential model

The same analysis was performed using the bi-exponential fitting model. In this case, four parameters must be estimated at the time: $T^*_{2,\texttt{fast}}$, $T^*_{2,\texttt{slow}}$, the signal amplitude S_0, and the fast signal fraction f. Compared to the mono-exponential case, the fitting problem is therefore significantly more complex.

For these simulations, a lower gaussian noise level of $\sigma_{gauss} = 3$ was used, corresponding to an SNR of approximately 66. Although this SNR is considerably higher than values typically encountered in sodium MRI phantom acquisitions, preliminary simulations using $\sigma_{\texttt{gauss}} = 30$ produced unstable parameter estimations, with distributions frequently reaching the imposed fitting boundaries or becoming nearly uniform. In section 3.1.2, the impact of $\sigma_{\texttt{gauss}}$ on model prediction will be described in details. Increasing the SNR was therefore necessary in order to evaluate the intrinsic behavior of the fitting model under favorable conditions. These observations already highlight one of the major limitations of bi-exponential fitting in ^{23}Na MRI. Because sodium imaging inherently suffers from low SNR, the simultaneous estimation of multiple relaxation parameters remains highly sensitive to noise.

The influence of the TE range is considerably more pronounced for the bi-exponential model. Figures 3.3a and d, corresponding respectively to the fast relaxation component

and the signal amplitude, show relatively similar distributions for both TE ranges. In contrast, Figures 3.3b and c reveal substantial differences for the slow relaxation component and the fast signal fraction.

Using the shorter TE range results in an underestimation of the slow T_2^* component, manifesting as a degradation of the distribution of the fraction parameter f. This behavior would be explained by the incomplete sampling of the slower decay component. Since the acquisition ends at 10.5 ms, a large part of the slow decay is not captured, which biases the fitting to predominantly take into account the shorter relaxation times. As a consequence, the contribution of the fast component becomes artificially overestimated, increasing the estimated mean value of f.

The corresponding R^2 distributions are presented in Figure 3.4. As expected, the 80 ms range provides better fitting performance, with distributions strongly concentrated around $R^2 = 1$. Nevertheless, the 10.5 ms range still produces relatively high R^2 values despite incorrect parameter estimation. This behavior illustrates one of the main limitations of multi-parameter fitting models: several combinations of parameters can generate nearly identical signal evolutions, leading to good fitting metrics despite inaccurate physical estimations. Consequently, caution is required when interpreting bi-exponential fitting results.

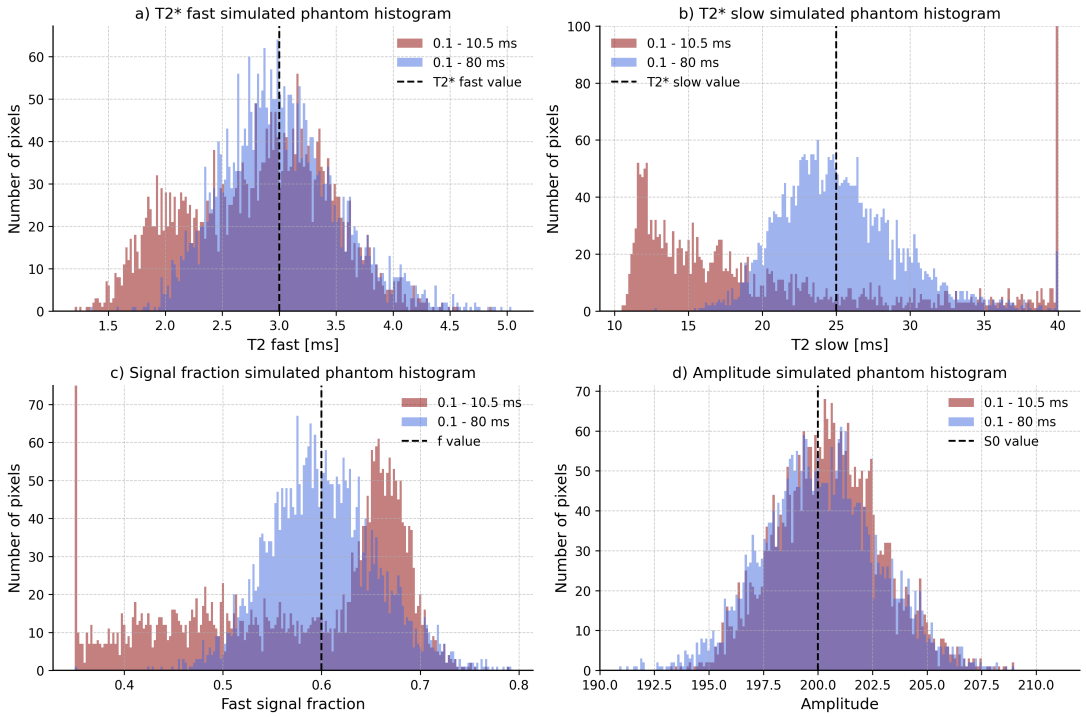

Figure 3.3: Parameter distributions obtained with the bi-exponential model using different echo ranges for the simulated phantom.

Based on these observations, the 80 ms TE range was selected for all subsequent simulated phantom experiments in order to maximize the accuracy of the parameter estimation.

3.1.2 Impact of noise level on parameter estimation

As previously discussed, the level of noise directly affects the SNR and therefore the stability and precision of the fitting procedure. The purpose of this section is to evaluate

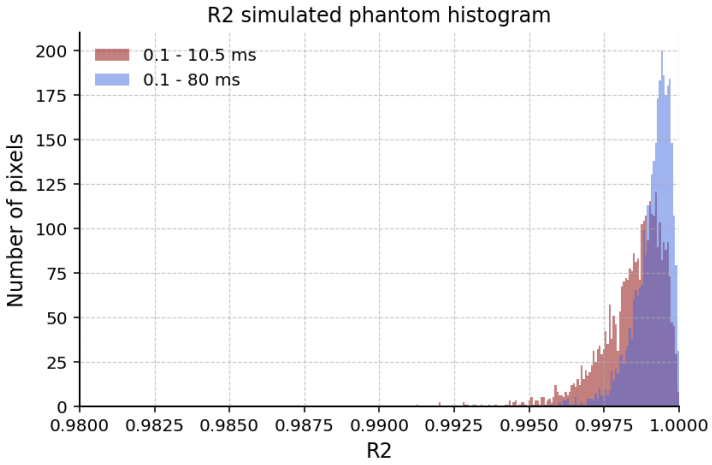

Figure 3.4: R^2 distributions obtained with the bi-exponential model using different echo ranges for the simulated phantom.

the sensitivity of both fitting models to noise and to identify their respective limitations. The echo range used for these simulations were based on the results from the section 3.1.1, and was set to 80 ms over 8 echos. Intuitively, the bi-exponential model is expected to be more sensitive to noise because of its larger number of free parameters. In such cases, even small perturbations in the signal may lead to very different parameter combinations producing similar fitting curves and comparable R^2 values.

Mono-exponential model

According to Section 2.4.1, Rician noise was introduced using:

$$\sigma_{\texttt{rician}} = \sigma_{\texttt{gauss}} \sqrt{\frac{\pi}{2}} \tag{3.1}$$

where σ_{gauss} corresponds to the standard deviation estimated form the experimental data using the SIS method.

The simulated phantom data were generated using $\sigma_{\texttt{gauss}} = 3$, 30, and 60. The corresponding parameter histograms for T_2^* and S_0 are shown in Figures 3.5a and b, while the associated R^2 distributions are presented in Figure 3.6.

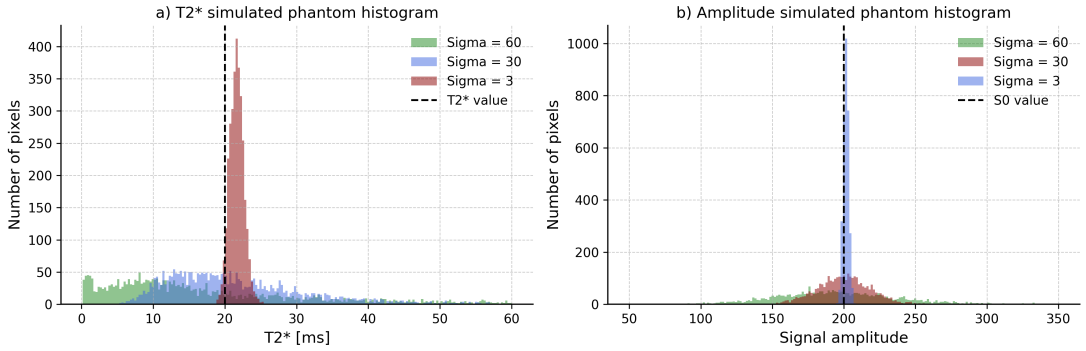

Figure 3.5: Parameter distributions obtained using the mono-exponential model on simulated phantom for different values of $\sigma_{\texttt{gauss}}$.

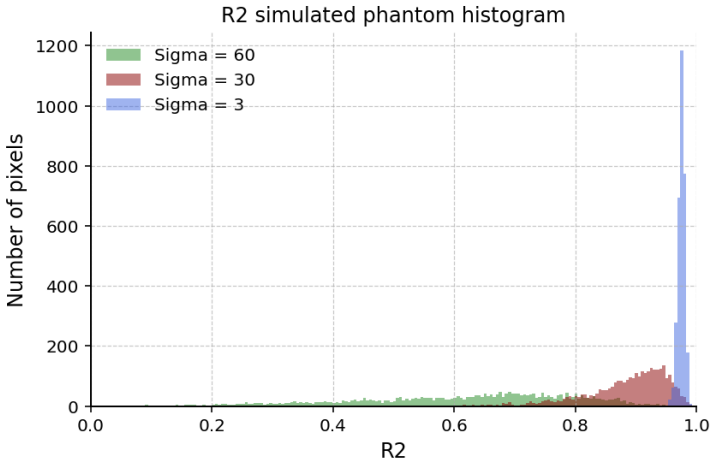

Figure 3.6: R^2 distributions obtained using the mono-exponential model on simulated phantom for different values of $\sigma_{\texttt{gauss}}$.

The results for mono-exponential model clearly demonstrate the impact of noise on the fitting accuracy. Low noise levels produce narrow parameter distributions centered around the expected values, whereas increasing noise progressively broadens the distributions. In particular, the case $\sigma_{\texttt{gauss}} = 60$ leads to a substantial spread in the estimated parameters together with an underestimation of the transverse relaxation time.

The R^2 distributions confirm this tendency. At low noise levels, the distributions are sharply concentrated near the optimal value $R^2 = 1$, indicating excellent fitting quality. As the noise level increases, the distributions become broader and shift toward lower values, reflecting the degradation of the fitting accuracy.

Bi-exponential model

The same analysis was performed using the bi-exponential fitting model with $\sigma_{gauss} =$ 1, 3, and 10. Figures 3.7 and 3.8 present the distributions of the estimated parameters and the corresponding R^2 values for the different noise conditions. As expected, increasing $\sigma_{\texttt{gauss}}$ progressively degrades the parameter estimation. This effect is particularly pronounced for the slow relaxation component $T^*_{2,\texttt{slow}}$ and the signal fraction f, whose distributions become increasingly broaded and eventually accumulate near the imposed fitting boundaries. In case of high level of noise, the distributions even approach a nearly uniform shape, indicating a loss of fitting stability. In contrast, the estimation of S_0 remains relatively robust, with mean values remaining close to the expected amplitude despite the increase in noise. This behavior is consistent with the fact that the signal amplitude is generally less sensitive to noise than the relaxation parameters. The estimation of the fast component T^*_{2fast} remains overall acceptable, a slight underestimation can be observed as the noise level increases.

The corresponding R^2 distributions shown in Figure 3.8 confirm that lower noise levels lead to improved fitting accuracy, with distributions becoming more concentrated around $R^2 = 1$. Nevertheless, relatively high R^2 values are still obtained even for the largest noise levels, despite the incorrect estimation of several parameters. This behavior highlights one of the main limitations of bi-exponential fitting: different combinations of parameters can generate very similar signal decay curves. Since the fitting procedure minimizes the mean squared error between the measured and simulated signals, the optimization can

converge toward incorrect parameter combinations while still producing apparently good fits according to the R^2 metric.

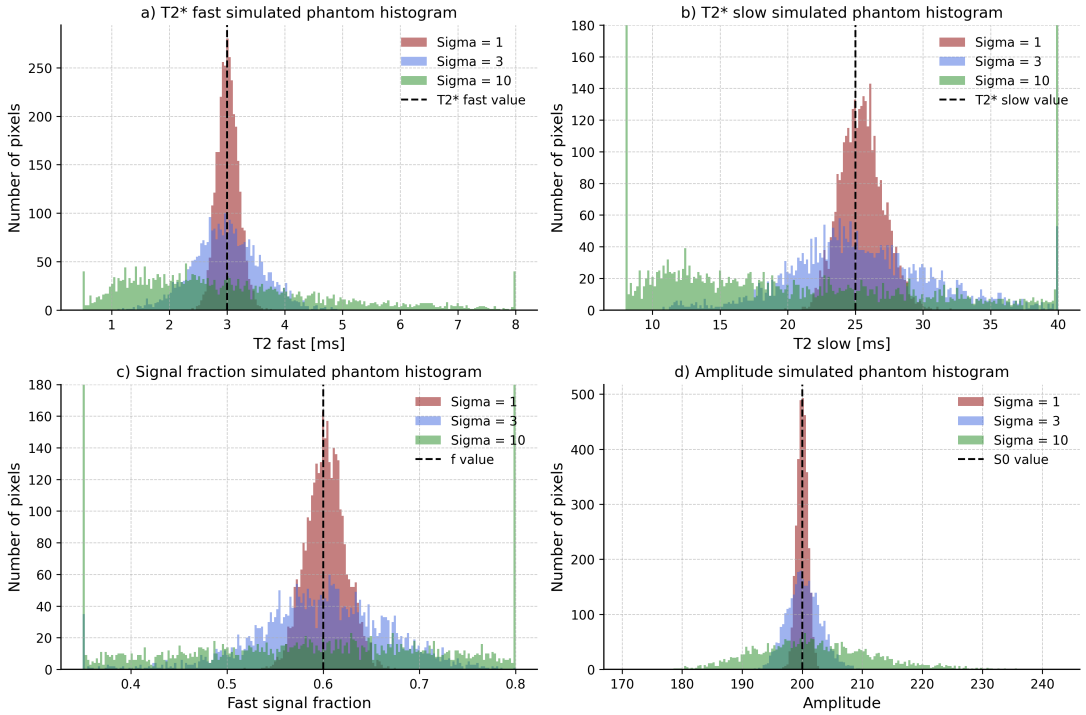

Figure 3.7: Parameter distributions obtained using the bi-exponential model on simulated phantom for different values of $\sigma_{\texttt{gauss}}$.

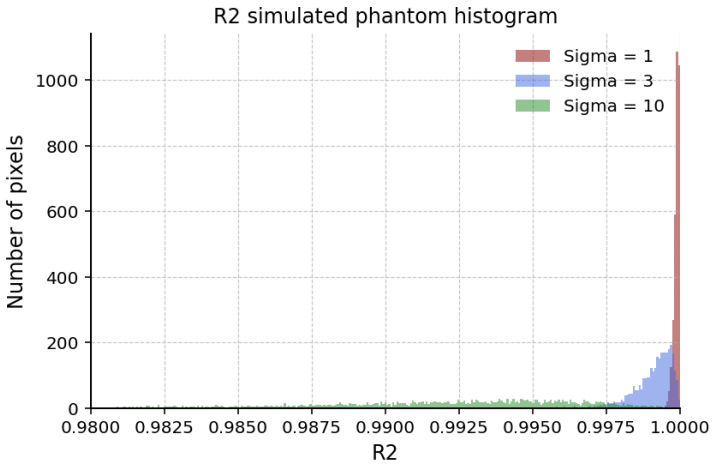

Figure 3.8: R^2 distributions obtained using the bi-exponential model on simulated phantom for different values of $\sigma_{\texttt{gauss}}$.

These results demonstrate that noise plays a critical role in bi-exponential fitting, especially in sodium MRI where the SNR is limited. Because the model relies on four interdependent parameters, the fitting process becomes highly sensitive to noise and parameter coupling. Consequently, bi-exponential fitting results should be interpreted carefully, as good R^2 values do not necessarily guarantee accurate parameter estimation.

3.1.3 Accuracy of parameter estimation

The simulated phantoms were also used to evaluate the accuracy of the fitting models in conditions representing the experimental setup.

Mono-exponential model

The parameter distributions are presented in Figure 3.9, and the expected parameter values are summarized in Table 2.4. The simulated phantom represents a homogeneous sodium solution, for which a mono-exponential decay is expected. .

Figures 3.9a and b present the distributions of T_2^* and S_0 obtained using a single set of parameters across the entire phantom volume. The resulting histograms are relatively narrow and centered around the expected parameter values, demonstrating that the mono-exponential model is capable of correctly estimating the relaxation properties under homogeneous conditions.

The second experiment was performed using two distinct sets of parameters in order to divide the phantom into two separate regions with different relaxation and concentration properties. The corresponding results are shown in Figures 3.9c and d. The estimation of the signal amplitude remains accurate, whereas the T_2^* distributions become broader and slightly less distinct. Nevertheless, the fitted values remain close to the expected parameters.

The associated R^2 distributions are shown in Figure 3.10. Both simulations produce similar fitting quality, although the two-region phantom exhibits slightly better results. This difference may be explained by the broader distribution observed in Figure 3.9a, where the homogeneous case exhibits a larger spread toward higher T_2^* values for a single value. In contrast, the second simulation includes expected relaxation times centered around 15 and 25 ms, which may overlap the distributions of the two datasets and increase the R^2 even if the estimated parameters are not the expected ones.

Bi-exponential model

Similar experiments were performed using the bi-exponential fitting model. Homogeneous and heterogeneous simulated phantoms were generated with the parameters summarized in the second part of Table 2.4. The corresponding parameter distributions obtained via fitting are presented in Figures 3.11a–h. A gaussian noise level of $\sigma_{\texttt{gauss}} = 3$ was selected in order to obtain sufficiently stable estimations.

The results obtained with a single parameter set are shown in Figures 3.11a–d for $T^*_{2,\texttt{fast}}$, $T^*_{2,\texttt{slow}}$, f, and S_0, respectively. As expected for a homogeneous phantom, the distributions remain centered around the theoretical values. However, even at this relatively low noise level, the histograms corresponding to $T^*_{2,\texttt{slow}}$ and f frequently reach the fitting boundaries, indicating that the model remains unstable and highly sensitive to noise, as exposed in the previous section.

The limitations of the model become more evident when two different regions are introduced into the phantom. Figures 3.11e–h show that the estimations of the slow relaxation component and the signal fraction become strongly biased. In particular, both parameters tend to be underestimated, leading to inaccurate characterization of the simulated regions. In contrast, the estimation of the fast relaxation component and the signal

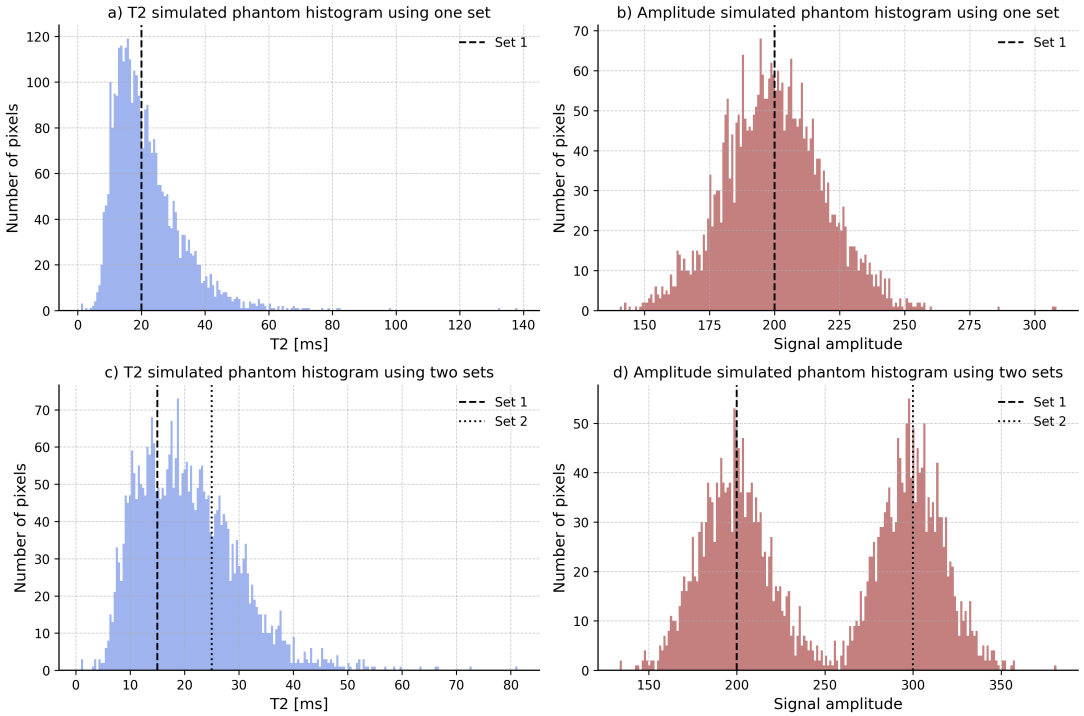

Figure 3.9: Parameter distributions obtained using the mono-exponential model on a)–b) homogeneous and c)–d) heterogeneous simulated phantoms.

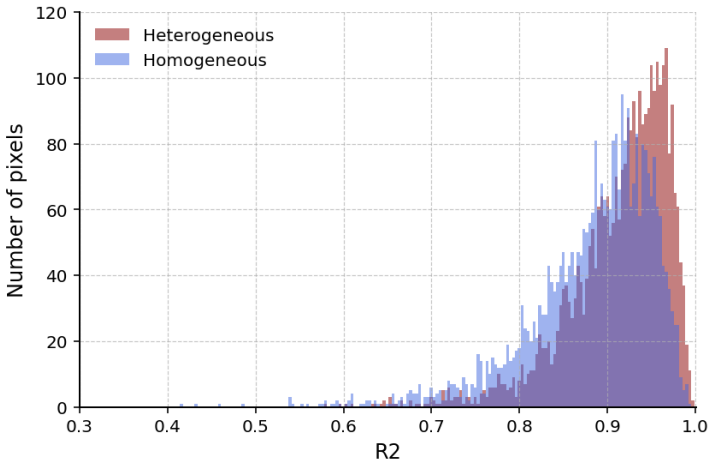

Figure 3.10: R^2 distributions obtained using the mono-exponential model on homogeneous and heterogeneous simulated phantoms.

amplitude remains comparatively more stable, although the fitted $T^*_{2,\texttt{fast}}$ values are still slightly underestimated. These results are confirmed to be less accurate according to the R^2 distributions in Figure 3.12.

These results demonstrate that the bi-exponential fitting model remains highly unstable even under artificially favorable SNR conditions compared to realistic sodium MRI acquisitions. The model frequently converges toward incorrect parameter combinations, particularly when several regions with different relaxation properties are present. This limitation may become problematic for both phantom and *in vivo* applications. Although phantoms are expected to be homogeneous, acquisition-related artifacts may still introduce intensity variations across the image.

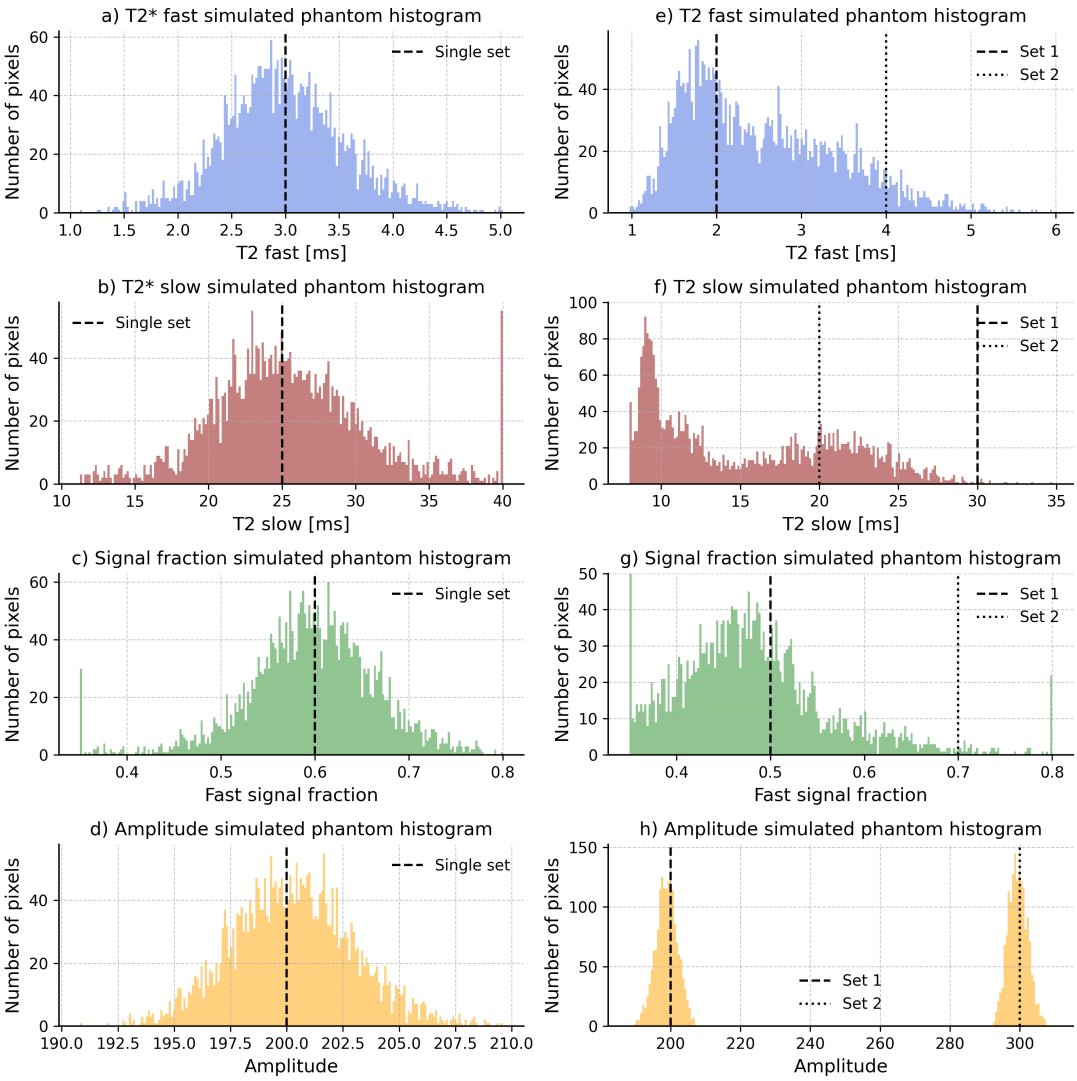

Figure 3.11: Parameter distributions obtained using the bi-exponential model on a)–d) homogeneous and e)–h) heterogeneous simulated phantoms.

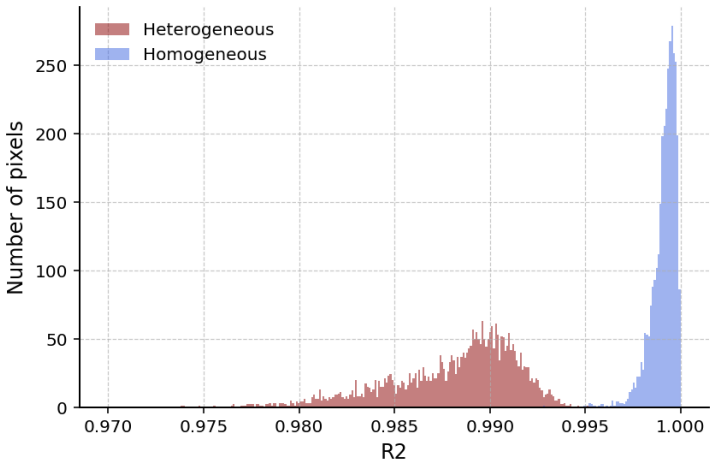

Figure 3.12: R^2 distributions obtained using the mono-exponential model on homogeneous and heterogeneous simulated phantoms.

In the human brain, the situation will be even more complex since different tissues exhibit distinct sodium concentrations and relaxation behaviors, while tissue boundaries

are not always sharply defined.

Overall, these observations suggest that bi-exponential fitting may be difficult to apply reliably to real sodium MRI data. Consequently, the interpretation of the following experimental results must be performed with caution.

3.1.4 Mono-exponential versus bi-exponential model analysis

The sodium MR signal in biological tissues is generally characterized by a bi-exponential decay, unless in regions exhibiting no complex microstructure such as the CSF that are represented by mono-exponential relaxation behavior. However, fitting a bi-exponential model remains challenging because several parameters must be estimated simultaneously. Although the mono-exponential approximation does not fully describe the underlying signal behavior in tissues, it offers important advantages in terms of computational simplicity, fitting stability, and processing time. This section therefore evaluates the differences between mono- and bi-exponential fitting in order to quantify the error introduced when a mono-exponential model is applied to data characterized by a bi-exponential decay.

To investigate this effect, simulated phantom data were generated using a bi-exponential signal model with the following parameters: $T^*_{2,\texttt{fast}} = 3$ ms, $T^*_{2,\texttt{slow}} = 25$ ms, $S_0 = 200$, $f = 0.6$ and $\sigma_{\texttt{gauss}} = 3$. Both mono-exponential and bi-exponential fitting procedures were applied to the same simulated dataset. The corresponding parameter distributions and R^2 values are presented in Figure 3.13. Figure 3.13a compares the estimated T^*_2 values for both models, T^*_2 from the mono-exponential model and $T^*_{2,\texttt{fast}}$ and $T^*_{2,\texttt{slow}}$ for the bi-exponential one. Figure 3.13b illustrates the associated R^2 distributions.

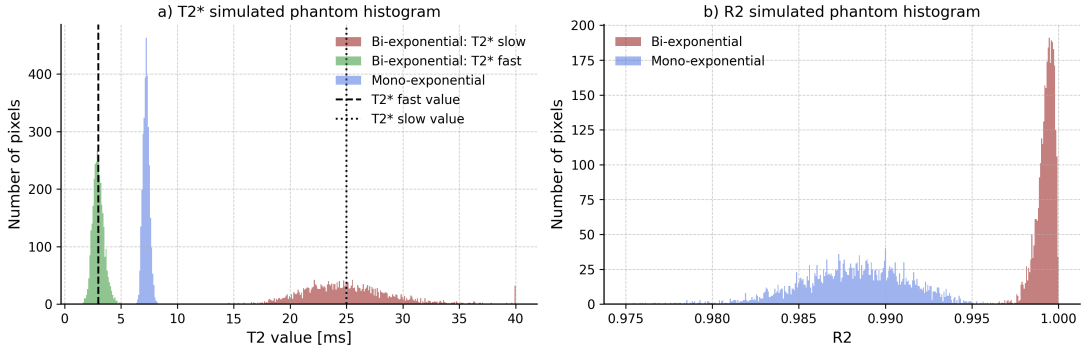

Figure 3.13: Comparison between mono- and bi-exponential fitting applied to simulated bi-exponential decaying phantom data.

The results clearly show that the mono-exponential model does not accurately reproduce the behavior of the simulated decay. While the true relaxation components were fixed at 3 ms and 25 ms, the mono-exponential fitting estimated a single T^*_2 value of approximately 7 ms. This estimated value lies much closer to the fast relaxation component than to the slow one, indicating that the mono-exponential approximation mainly captures the initial part of the decay curve.

This behavior can be further observed in Figure 3.14, which compares representative fitting curves obtained using both models. The bi-exponential fit reproduces the simulated signal much more accurately, particularly at low noise levels. In contrast, the mono-exponential model primarily follows the rapid initial signal decrease and fails to properly characterize the slower decay component. This explains why the estimated

mono-exponential T_2^* value is biased toward the fast relaxation time.

The differences between both approaches are also reflected in the R^2 distributions shown in Figure 3.13b. The bi-exponential model produces distributions strongly concentrated near to 1, indicating excellent agreement between the model and the simulated data. Conversely, the mono-exponential model yields broader and lower R^2 distributions, confirming the reduced fitting accuracy associated with this simplified representation of the signal decay.

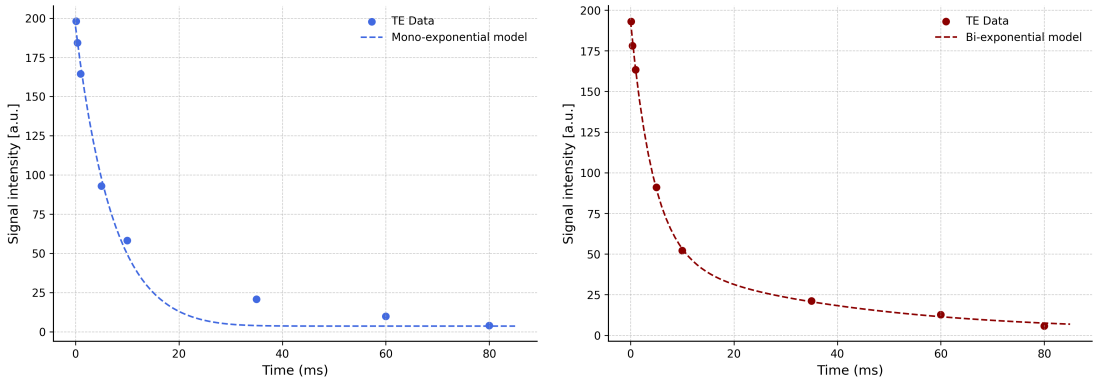

(a) Mono-exponential model (b) Bi-exponential model

Figure 3.14: Example of mono-exponential and bi-exponential fitting curves obtained from simulated bi-exponential phantom data.

3.2 SNR optimization results

Optimizing the signal-to-noise ratio is a major challenge in sodium MRI because of the low MR signal intensity generated by sodium nuclei. In this work, two constraints were introduced into the SNR optimization model in order to maintain clinically acceptable acquisition durations while remaining within SAR safety limits.

The first constraint relates the acquisition time to the repetition time and the number of projections:

$$\mathrm{TA} = N_p \cdot \mathrm{TR} \tag{3.2}$$

The second constraint describes the dependence of SAR on flip angle and repetition time:

$$\mathrm{SAR} \propto \frac{\mathrm{FA}^2}{\mathrm{TR}} \tag{3.3}$$

Combining these relationships with the SNR expression introduced previously led to the following optimization model:

$$\mathrm{SNR}(\mathrm{TR}) \propto \frac{\sin\left(\sqrt{\mathrm{SAR}\cdot\mathrm{TR}}\right)\left(1-e^{-\mathrm{TR}/T_1}\right)}{1-\cos\left(\sqrt{\mathrm{SAR}\cdot\mathrm{TR}}\right)e^{-\mathrm{TR}/T_1}}\sqrt{\frac{\mathrm{TA}}{\mathrm{TR}}} \tag{3.4}$$

The objective was to maximize the equation 3.4 with respect to the repetition time using phantom acquisitions while respecting both acquisition time and SAR limitations.

The experimental measurements confirmed the theoretical relationships between SAR, repetition time, flip angle, number of projections, and SNR, as illustrated in Figure 3.15. Figure 3.15a shows the expected inverse relationship between SAR and repetition time described by equation 3.3. Short repetition times produced higher SAR values because RF excitation pulses were applied more frequently during the acquisition. Similarly, Figure 3.15b confirms the quadratic dependence of SAR on the flip angle. Increasing the flip angle substantially increased SAR values in both phantom and *in vivo* measurements, in agreement with the theoretical model. The dependence of SNR on the number of radial projections is presented in Figure 3.15c. As expected, the measured SNR increased proportionally to the square root of the number of projections, validating the theoretical prediction in equation 3.4.

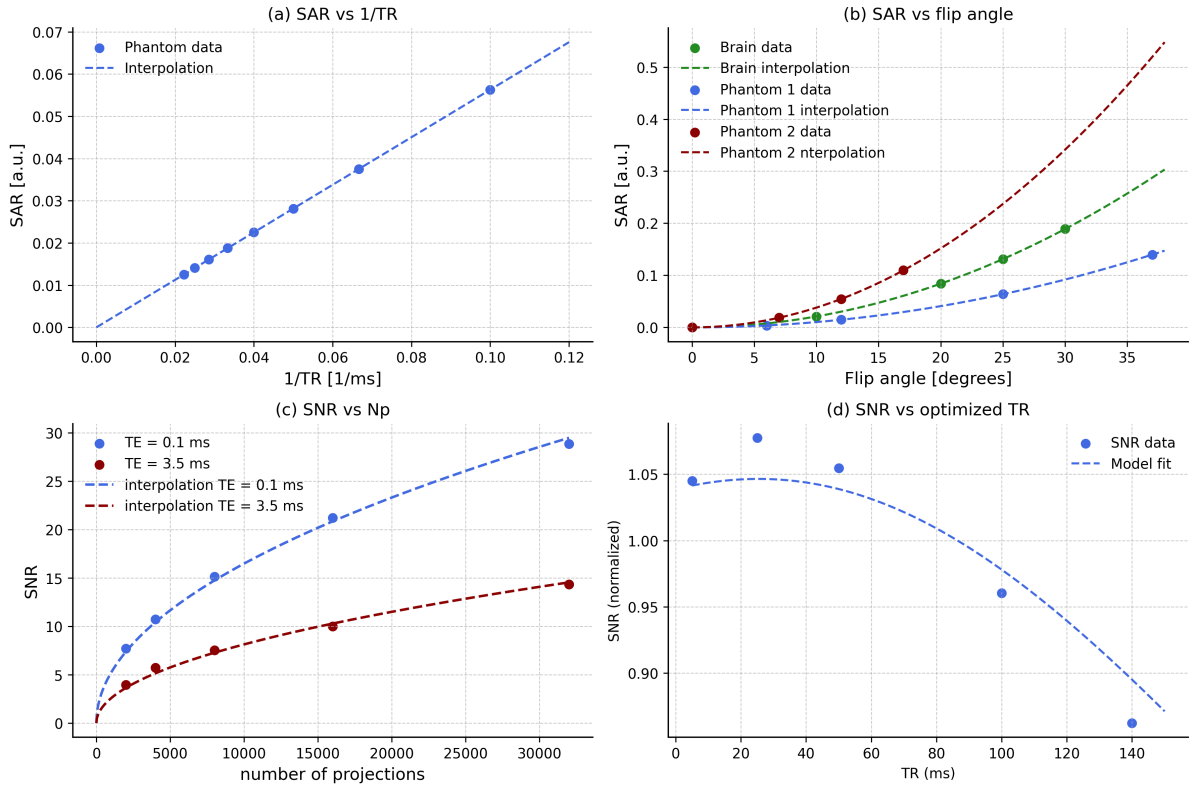

Figure 3.15: Results of the SNR optimization experiments. a) SAR as a function of 1/TR. b) SAR as a function of the applied flip angle. c) SNR as a function of the number of radial projections. d) Comparison between theoretical and measured SNR values as a function of repetition time. Experimental and theoretical values were normalized to their mean for comparison purposes.

The numerical optimization identified an optimal repetition time of 25 ms under the imposed SAR and acquisition time constraints for scan parameters described in Table 2.1. The corresponding optimized acquisition parameters were:

$$\text{TR} = 25 \text{ ms}, \qquad \text{FA} = 38^\circ, \qquad N_p = 14722 \text{ projections} \tag{3.5}$$

The experimentally measured SNR values followed the same general trend as the theoretical predictions across the investigated repetition times. Table 3.1 summarizes the acquisition parameters together with the corresponding mean signal intensity, standard deviation, and measured SNR values.

Among all tested configurations, the optimized acquisition obtained at TR = 25 ms indeed produced the highest measured SNR. This acquisition reached approximately 93.8% of the theoretically predicted SNR expected for an Ernst-angle acquisition acquired under identical acquisition time and TR conditions. In addition, the optimized acquisition systematically outperformed the suboptimal conditions tested at different TR under similar total acquisition time and SAR constraints. These results demonstrate that the optimization model provides a reliable framework for selecting sodium MRI acquisition parameters under practical experimental constraints.

Finally, Figure 3.15d compares the theoretical and experimentally measured SNR evolutions as a function of repetition time. The measured values follow the predicted trend, confirming the validity of the optimization approach. The curves were normalized to the mean experimental SNR in order to facilitate the comparison between measured and theoretical values.

Scans	**TR (ms)**	**FA (degrees)**	N_p	**Mean**	σ_{gauss}	**SNR**
Optimized scan	25	38	14722	900.02	35.06	16.81
Scan 1	5	17	73600	1946.19	78.52	16.23
Scan 2	50	53	7396	618.53	24.97	16.22
Scan 3	100	76	3684	402.21	17.76	14.83
Scan 4	140	90	2632	302.4	14.76	13.41

Table 3.1: Summary of the SNR optimization experiments and corresponding acquisition parameters.

It is important to note that this optimization has its applicability limits. If larger TR values are needed (e.g., for increased TE range, as described in Section 3.1.1), this method is not optimal with similar SAR and total scan duration. Indeed, as SAR constraint is alleviated, Ernst angle acquisitions become possible. Meanwhile, due to total time constraint, the number of projections related to the acquisition time decreases with increasing TR, leading to the degradation of the resulting SNR.

3.3 T_1 estimation results

The T_1 maps were generated using the variable flip angle (VFA) method by fitting the steady-state transverse magnetization acquired with different flip angles. Both UTE and DARAD sequences were investigated.

$$M_{xy}(\text{FA}) = M_0 \frac{1 - e^{-\text{TR}/T_1}}{1 - \cos(\text{FA}) e^{-\text{TR}/T_1}} \sin(\text{FA}) \tag{3.6}$$

Equation 3.6 was fitted voxel-wise within the selected mask in order to generate the corresponding T_1 relaxation maps in both phantoms and human brain data.

3.3.1 Phantom T_1 maps

The signal amplitude parameter S_0 was not directly compared between the two acquisition sequences because UTE and DARAD reconstructions do not share the same signal scaling. Consequently, differences in absolute S_0 values are not meaningful in this context. Nevertheless, the spread of the S_0 distributions remains informative but won't be analyzed.

In a homogeneous phantom, the T_1 relaxation time is expected to remain approximately constant throughout the entire volume. However, there is no ground truth for T_1 value to reference. As a result, it is not possible to determine whether the estimated distributions are really centered around the true relaxation value. For this reason, the analysis focuses not only on the estimated T_1 distributions but also on the associated R^2 values, as exposed in section 2.3.

The comparison between UTE and DARAD acquisitions is presented in Figure 3.16. A clear difference can be observed between both sequences. The DARAD acquisition produces narrower T_1 distributions and significantly higher R^2 values than the UTE sequence. In particular, the DARAD R^2 histogram exhibits a strong concentration near $R^2 = 1$, indicating improved fitting accuracy and better model stability. In contrast, the UTE sequence produces broader parameter distributions and slightly shifted T_1 values, suggesting a tendency to overestimate the relaxation time compared with DARAD measurements.

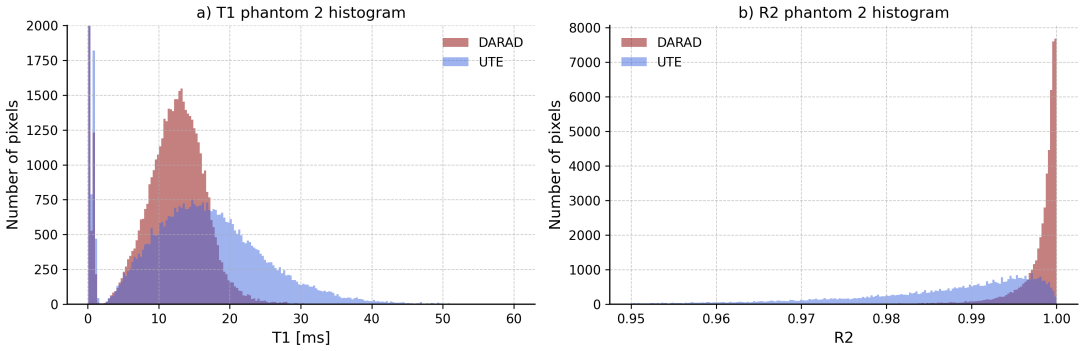

(a) T_1 and R^2 histograms for phantom 2 T_1 mapping

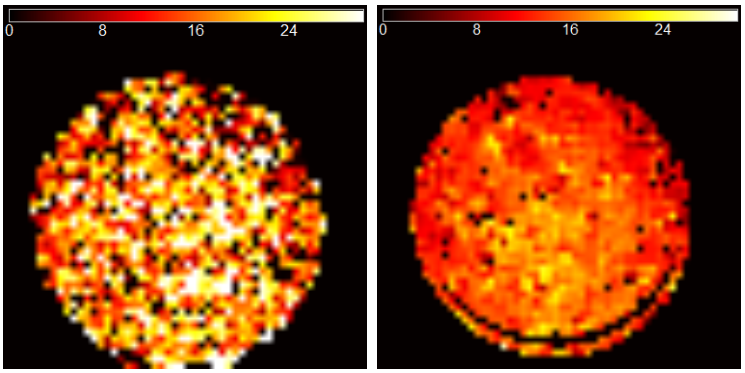

(b) UTE T_1 map (ms) (c) DARAD T_1 map (ms)

Figure 3.16: T_1 and R^2 histograms with the corresponding phantom T_1 maps obtained using UTE (blue) and DARAD (red) sequences.

Figures 3.16b and 3.16c illustrate representative slices of the phantom T_1 maps obtained using the UTE and DARAD sequences, respectively. The DARAD acquisition

produces a much more homogeneous relaxation map, whereas the UTE map exhibits stronger local fluctuations and less spatial uniformity. These observations further support the improved robustness of the DARAD sequence for quantitative T_1 estimation.

3.3.2 Human brain T_1 maps

Figure 3.17a presents the histogram distributions of the estimated T_1 and S_0 values within the brain mask. After brain extraction, the fitting procedure was applied only to voxels belonging to brain tissues. The resulting mean T_1 value over the entire brain, including white matter, gray matter and CSF, was approximately 55 ms. This estimated value is noticeably higher than the 44.1 ms value reported in the literature [15]. Something that may explain this difference could be that the number of flip angles used for the VFA fitting remained limited, which may reduce the robustness of the estimation. The possibility that the larger T_1 expressed in the CSF shifts the distribution toward higher T_1 values must be considered as well.

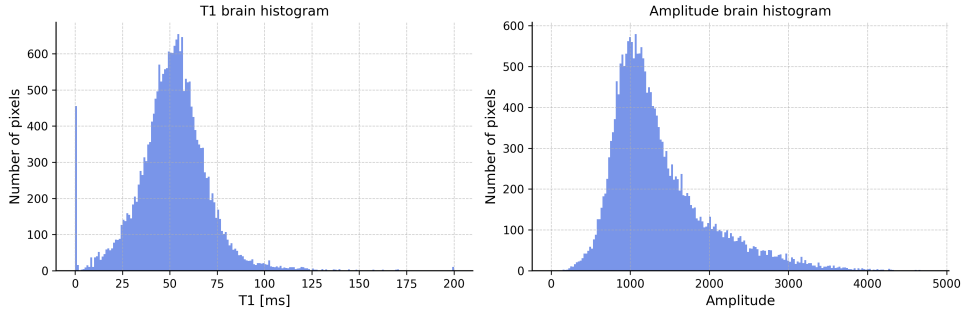

(a) T_1 and S_0 brain histograms

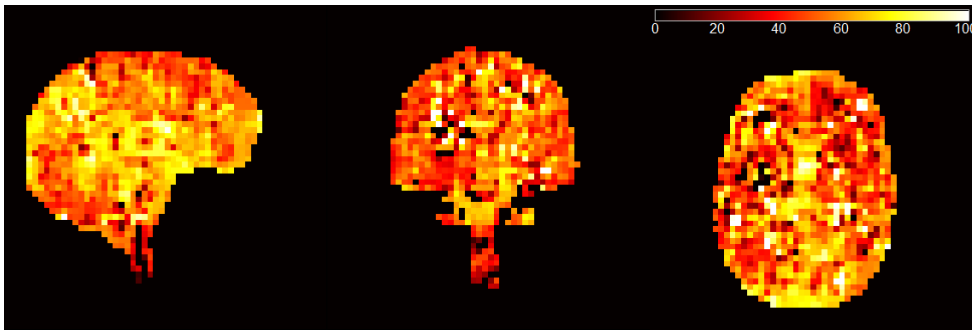

(b) T_1 map of the brain (ms)

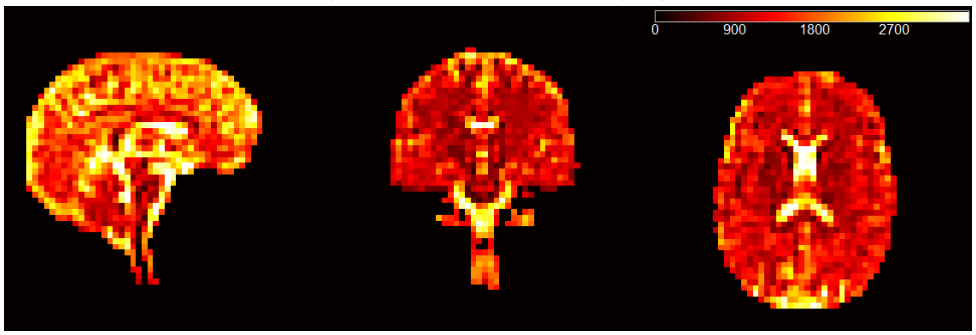

(c) S_0 map of the brain (a.u.)

Figure 3.17: T_1 and S_0 histograms with the corresponding brain maps obtained using the VFA method.

Figures 3.17b and 3.17c present representative slices of the estimated T_1 and S_0 maps, respectively. The signal amplitude map clearly highlights anatomical structures within

the brain. In particular, CSF regions are well identified because of their higher sodium concentration compared with surrounding tissues. In contrast, the T_1 map appears considerably less structured. Distinct anatomical regions are difficult to identify, suggesting that the VFA fitting procedure does not estimate the relaxation parameter with sufficient precision under the current acquisition conditions. This limitation likely results from the strong sensitivity of the VFA method to signal fluctuations and noise.

Figure 3.18a illustrates an example of the voxel-wise fitting procedure performed during the VFA estimation. Small deviations in one or more signal points can substantially alter the estimated T_1 value, demonstrating the instability of the fitting process. The corresponding R^2 distribution in Figure 3.18b shows relatively good fitting accuracy. This would include that the model is more sensitive to noise because any disruption of the signal for a specific flip angle could lead to the mis-estimation of T_1, which would be avoided if more flip angle images were acquired. This would stabilize the fitting by increasing the sampling, decreasing the effect of a single noised voxel on the global estimated parameters.

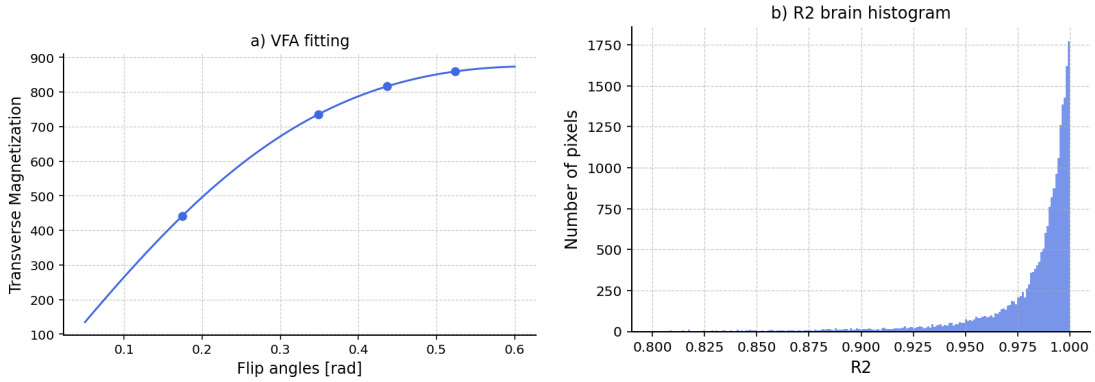

Figure 3.18: Example of voxel-wise VFA fitting with the associated R^2 distribution obtained for human brain T_1 mapping.

3.4 T_2^* estimation results

Similarly to section 3.3 related to T_1 estimation, the SNR optimization results presented in section 3.2 were not used for the following experiments. Indeed, accurate T_2^* mapping requires a large echo time range extending from 0.15 ms to 80 ms, as demonstrated by the simulated phantom results in section 3.1. Consequently, the repetition time cannot be reduced as much as in SNR optimization requires and must remain relatively long to allow the acquisition of all echoes.

In this section, the results obtained after the pre-processing steps described in section 2.4 for the T_2^* component estimation are presented, using both mono-exponential and bi-exponential fitting models.

3.4.1 Phantom T_2^* maps

This part only focuses on mono-exponential fitting applied to phantom acquisitions. Indeed, as the phantom consists of a homogeneous liquid gel solution containing water and sodium, the resulting sodium signal decay can reasonably be approximated using a

mono-exponential model.

Figure 3.19a presents the distributions of the estimated T_2^* values together with the corresponding R^2 histograms for both UTE and DARAD sequences. Once again, the DARAD sequence provides more reliable parameter estimation. Although both acquisition methods produce T_2^* distributions centered around a similar value of approximately 7 ms, both the spread of the T_2^* and R^2 distributions reveal a clear difference in fitting quality. The UTE acquisition leads to a much broader R^2 distribution, indicating reduced fitting stability and precision compared to DARAD. It is mainly expressed by the spread of the distribution, which is narrower for DARAD sequence compared to the one of UTE.

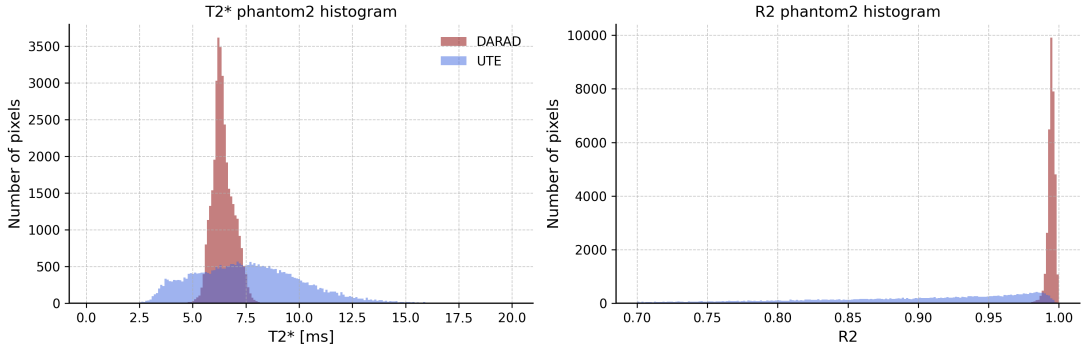

(a) T_2^* and R^2 phantom histograms

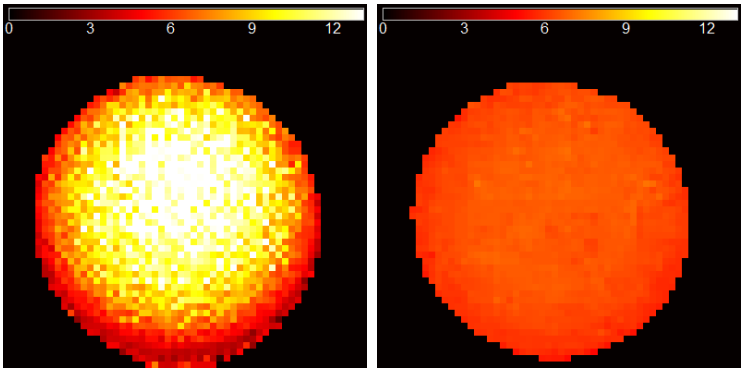

(b) UTE T_2^* map (ms) (c) DARAD T_2^* map (ms)

Figure 3.19: T_2^* and R^2 histograms with the corresponding mono-exponential T_2^* maps obtained in phantom 2 acquisitions using UTE and DARAD sequences.

This observation is further confirmed by the corresponding T_2^* maps shown in Figures 3.19b and 3.19c. The UTE map exhibits visible spatial inhomogeneities, with larger T_2^* values observed in the center of the phantom and lower values near the periphery. In contrast, the DARAD sequence produces a considerably more uniform distribution of T_2^* values across the entire phantom volume, which is more consistent with the expected homogeneous composition of the phantom.

3.4.2 Human brain T_2^* maps

Although sodium signal decay in human brain tissues is theoretically better characterized by a bi-exponential relaxation model, such a model remains difficult to fit reliably because it involves four interdependent parameters. It requires fitting voxel-wise the following equation:

$$S(t) = S_0(f e^{-t/T^*_{2,\mathrm{fast}}} + (1-f)\, e^{-t/T^*_{2,\mathrm{slow}}}) \tag{3.7}$$

As demonstrated in the simulated phantom experiments presented in Section 3.1, this complexity leads to large fitting instabilities and inaccurate estimations, particularly for the slow relaxation component and the fast signal fraction. For this reason, a mono-exponential fitting model was first applied to the human brain data using the following mono-exponential model:

$$S(t) = S_0\, e^{-t/T_2^*} \tag{3.8}$$

Similarly to the T_1 brain experiments, only DARAD acquisitions were performed because this sequence previously demonstrated better fitting stability and parameter estimation accuracy owing to increased SNR in phantom acquisitions.

Mono-exponential model

The distributions of the estimated T_2^* and R^2 for the mono-exponential fitting are presented in Figure 3.20a. The estimated T_2^* values range from a few milliseconds up to approximately 60 ms, which remains relatively consistent with values reported in the literature. In the work of Nagel et al. [15], T_2^* values up to approximately 50 ms were reported in cerebrospinal fluid, while lower values between 15 and 30 ms were observed in white and gray matter. Similar behavior can be observed in Figure 3.20b, although the estimated values in this thesis shows values between 10 and 35 ms in gray and white matter regions.

As expected, the S_0 map shown in Figure 3.20c provides a good representation of the anatomical structures of the brain. Several regions such as the CSF and the brain stem can be clearly distinguished because of their different sodium concentrations. In contrast, the T_2^* map exhibits lower structural contrast and appears a bit less segmented.

Bi-exponential model

The bi-exponential fitting procedure was applied voxel-wise in order to estimate the fast and slow transverse relaxation components of the sodium signal decay, with the corresponding fast signal fraction and signal amplitude parameters expressed in equation 3.7. Figure 3.21 presents the distributions of the estimated parameters obtained from the brain data, while Figure 3.22 shows the distribution of R^2.

The histogram of $T_{2,\texttt{fast}}^*$ shown in Figure 3.21a indicates that most estimated values are concentrated in the lower relaxation range, with a large proportion lower than approximately 4 ms. In addition, an accumulation of voxels near the upper and lower fitting boundary can be observed, which may suggest that the estimation of the fast component becomes unstable in low-SNR data.

The slow relaxation component histogram presented in Figure 3.21b shows a broader distribution centered around intermediate values. Most voxels are distributed between approximately 20 and 60 ms, which is consistent with the expected behavior of slowly relaxing sodium compartments in brain tissues [11]. However, fitting in a lot of voxels tends to converge to the upper boundary, indicating that certain regions may not provide sufficient information for reliable estimation of the slow component.

The fast signal fraction distribution shown in Figure 3.21c demonstrates that the estimated fractions are mainly distributed between 0.2 and 0.8, the imposed bounds, knowing the approximate through value of $f = 0.6$ in the whole brain. The estimation of

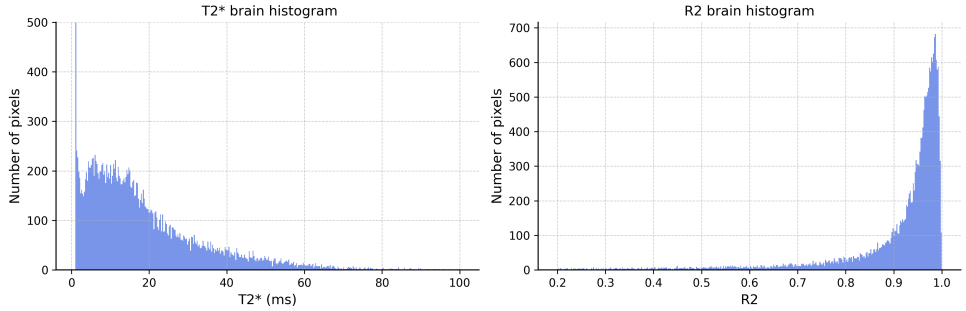

(a) T_2^* and S_0 histograms

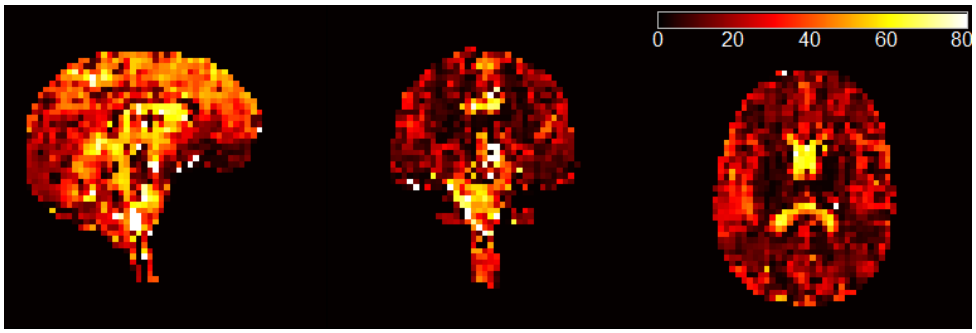

(b) T_2^* map of the brain (ms)

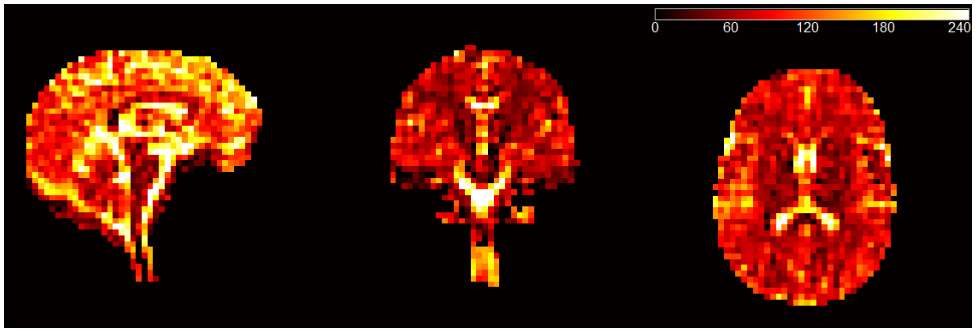

(c) S_0 map of the brain (a.u.)

Figure 3.20: T_2^* and S_0 histograms using the mono-exponential model and the corresponding maps of the brain

this parameter is really not precise as indicated by the broad distribution. The presence of voxels at the imposed boundaries also suggests sensitivity of the bi-exponential fitting procedure to noise.

The S_0 histogram in Figure 3.21d exhibits a more compact and physiologically coherent distribution. Most voxel amplitudes are concentrated around coherent intensity values, with progressively fewer voxels at lower and higher amplitudes. This observation confirms that the signal amplitude estimation remains more stable than the estimation of the other parameters for the bi-exponential model.

The distribution of R^2 shown in Figure 3.22 demonstrates generally high fitting quality for the majority of voxels. Most values are concentrated close to 1, indicating that the bi-exponential model adequately reproduces the variation in the measured signal. However, the broad distributions indicate that R^2 is not a proper metric for this fit, which is expected because the number of variables (4) was close to the number of measurements (8).

Overall, the bi-exponential model results demonstrate the possibility of estimating multi-component sodium relaxation parameters in the human brain. However, the broad

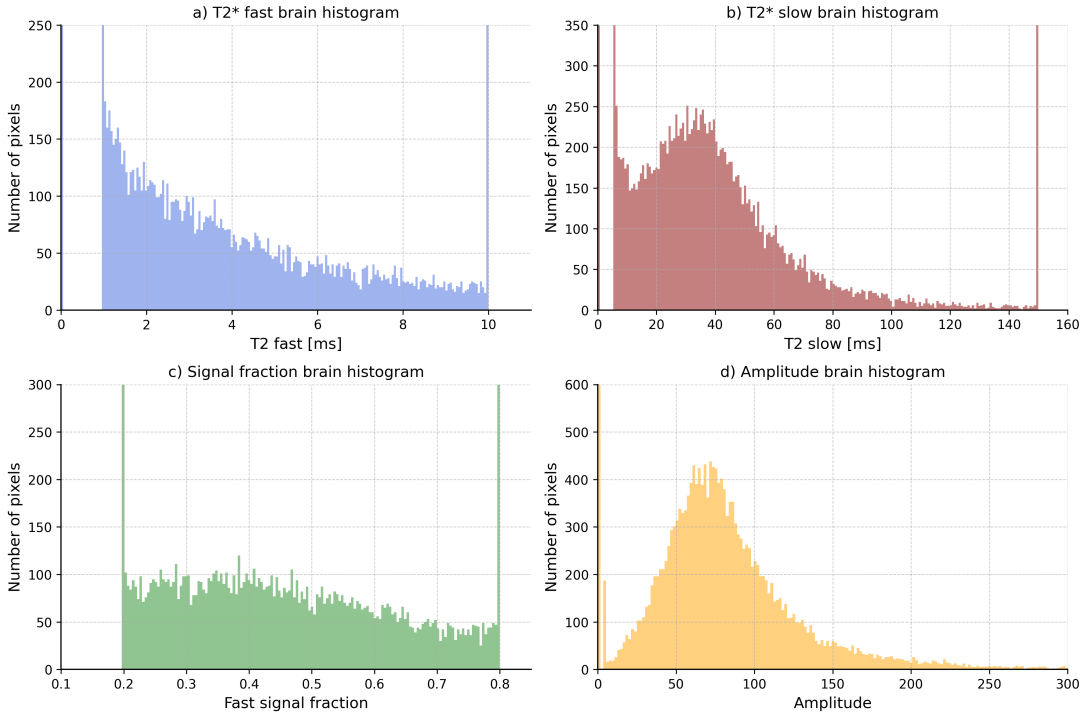

Figure 3.21: Parameter histograms using the bi-exponential model on human brain

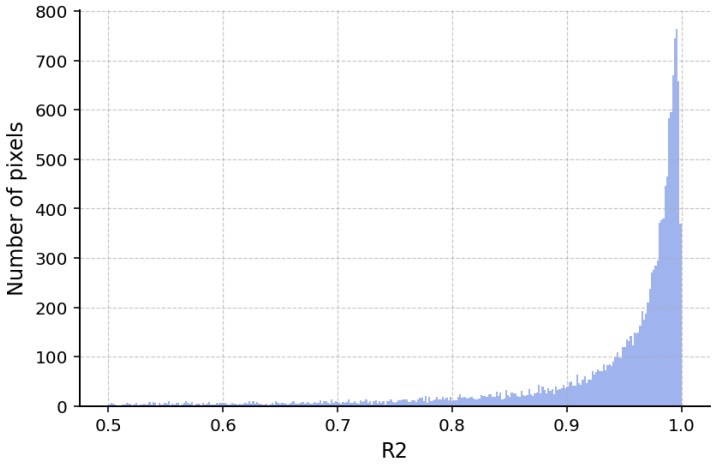

Figure 3.22: R^2 histograms using the bi-exponential model on human brain

parameter distributions and the presence of voxels reaching boundary values also highlight the sensitivity of the fitting procedure to noise and the need to further improve SNR and acquisition strategies.

Mono- and bi-exponential model comparison

This section compares the transverse relaxation time estimation obtained using mono-exponential and bi-exponential fitting models in human brain data. The objective was to evaluate whether the differences previously observed in the simulated phantom experiments are also present under realistic *in vivo* acquisition conditions. Figure 3.23 presents the distributions of the estimated T_2^* values and the corresponding R^2 for both fitting approaches.

The mono-exponential fitting produced a relatively broad distribution of T_2^* values

extending toward longer relaxation times. Its estimation shows a single effective relaxation component combining both fast and slow sodium signal contributions. In contrast, the bi-exponential model separated the signal decay into distinct fast and slow relaxation components. The fast component was concentrated at very short relaxation times, with most values distributed below approximately 10 ms because of the imposed bounds. The slow component exhibited a broader distribution extending toward longer relaxation times, with most voxels located between approximately 20 and 60 ms.

As expected with the imposed long and short fitting bounds, the separation of the two components demonstrates the ability of the bi-exponential model to capture more complex sodium relaxation behavior than the mono-exponential approximation. While the mono-exponential model provides a single averaged relaxation estimate, the bi-exponential approach allows the characterization of distinct signal decay regimes potentially associated with different sodium environments. However, the distributions obtained with the bi-exponential model also appear substantially broader and more heterogeneous than those obtained with the mono-exponential fitting. In particular, accumulations of voxels near the lower and upper fitting boundaries are visible for both fast and slow components, suggesting increased fitting sensitivity to noise and parameter instability. This behavior is maybe not fully captured using this system of bounds based on physiological values found in the literature and should be reviewed.

The distribution of R^2 for both fitting models achieve generally high values. Nevertheless, the bi-exponential model exhibits slightly higher concentrations of voxels around $R^2 = 1$ compared with the mono-exponential model. Despite this improved fitting quality, the higher variability observed in the estimated bi-exponential parameters indicates that better goodness of fit does not necessarily imply greater estimation robustness. The larger number of parameters generally induces larger R^2 but increases the sensitivity of the model to noise, parameter coupling and the choice of initial conditions.

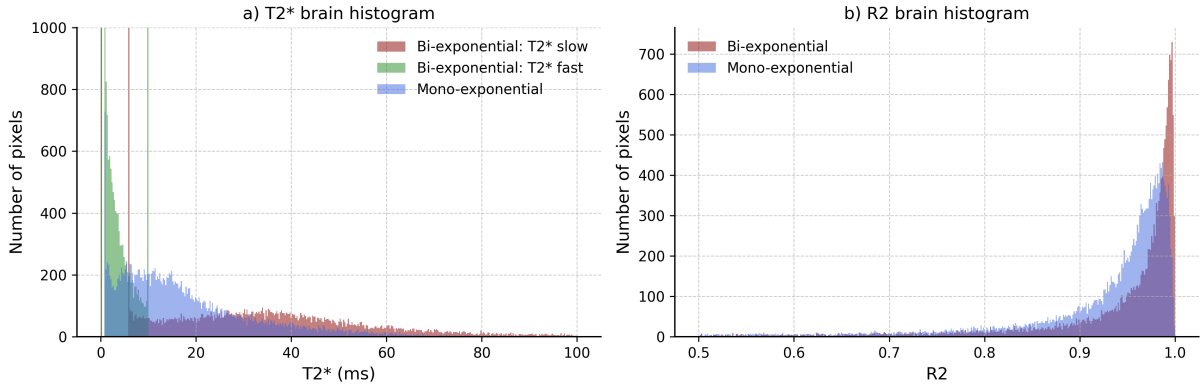

Figure 3.23: Comparison between mono- and bi-exponential fitting on human brain data

Overall, these results confirm the observations previously obtained in the simulation experiments 3.1.4. The bi-exponential model theoretically provides a more realistic description of sodium transverse relaxation behavior but remains substantially more sensitive to acquisition limitations and fitting instability than the mono-exponential approximation.

3.5 Abstract submission

The results related to the optimization of SNR in section 3.2 were submitted for the international 42nd annual meeting of the European Society for Magnetic Resonance in Medicine and Biology (ESMRMB 2026) in Spain. The submitted abstract is not yet accepted by the organizers of the event.

The abstract is available on ORBi[1], while the code used for the parameter optimization is accessible on one of CRC's GitHub repositories[2].

[1] https://hdl.handle.net/2268/345774

[2] https://github.com/CyclotronResearchCentre/SNRoptim_23NaMRI/

Chapter 4

Discussion

The objective of this thesis was to evaluate the feasibility of the generation of quantitative sodium MRI mapping at ultra-high field (7T) through the estimation of sodium relaxation properties in phantom and human brain data acquisition. Particular attention was placed on the influence of the choice of sequence types (UTE and DARAD), image quality and fitting accuracy for both T_1 and T_2^* parameter estimations, and to the comparison between the two possible strategies for the transverse relaxation time mapping: mono- and bi-exponential models.

The previous Chapter 3 demonstrated that the quantification in ^{23}Na MRI remains challenging because of the isotope properties such as the low gyromagnetic ratio, low *in vivo* concentration, and rapid transverse relaxation properties. However, the results showed that quantitative relaxation maps are possible through adequate fitting model.

This chapter will further discuss the results obtained on simulated phantoms for the analysis of the behavior of mono- and bi-exponential models, and both on phantoms and human brain data to have an idea of the real use and limitations of these estimations.

4.1 Influence of acquisition on quantitative mapping

4.1.1 Echo sampling strategy for T_2^* estimation

The range of echos was shown to have an important influence on fitting accuracy, especially for the bi-exponential model where the interdependency of the four parameters reduces the estimation precision. In fact, the simulation experiments demonstrated that the characterization of T_2^* of both very short and long echo acquisitions times is essential. This observation can be explained by the presence of fast and slow relaxation components, characterized by different regions in the signal decay. In particular, a larger number of points should be acquired at early echos to have a good estimate of the fast components within a few milliseconds.

The ideal set of echo times would be to sample a large number of echos from 0.1 to at least 80 ms, more than the 8 ones acquired for this work. However, this would increase the acquisition time required to generate a single relaxation map with similar image quality, which is not ideal for the comfort of the patient.

In the work of Ridley [11], 24 echos were performed in order to fully estimate the T_2^* signal decay for an acquisition time of 60 min. The trade-off between the number of echos and the acquisition time is then possible to reach in keeping the accuracy of the estimation on bi-exponential model parameters, even if 60 minutes for a single transverse relaxation map remains a long acquisition time. Such acquisition time might be acceptable for a slow dynamics applications, such as joints imaging, but might be less useful for a more dynamic brain scans.

4.1.2 Noise and SNR optimization

The results obtained in both simulations and experimental acquisitions demonstrated that SNR directly influences the reliability of quantitative fitting procedures. As noise levels increased, the variability of estimated parameters also increased. This effect was particularly visible for bi-exponential T_2^* parameter estimation, where noise mainly introduced uncertainty in the determination of the slow relaxation component and signal fraction. Then, the reliability of quantitative sodium MRI remains strongly dependent on the acquisition of sufficiently high-SNR data. Unfortunately, for sodium imaging, the range of acceptable SNR leading to relatively good estimation distribution is inaccessible with the current technology. Indeed, section 3.1.2 showed that the SNR for the bi-exponential fitting should be about 66 to obtain reliable parameter estimation under the conditions of this study. In the literature, the reachable sodium SNR at 7T in human brain is about 28.4 [24], which is far from the one obtained in this study.

The selection of tissue regions of interest in the gray matter, white matter and CSF can lead to more stable estimation of parameters. In fact, this could decrease the impact of noise in some parts of the brain that are not spatially well defined, leading to confusing regions and even maybe some artifact at the periphery of the brain or substructures. Different articles applied such a parcelation to evaluate the T_2^* components into well defined regions of the brain, leading to more precise and uniform estimation of parameters [11, 23].

However, the different distributions demonstrated in this work were plotted for the whole brain volume. Some interesting results would be generated in selecting such regions of interest in the white, gray matter and CSF, to allow easier histogram analysis and more comparable fitting data decay. The spatial resolution should maybe be increased in order to get more estimation points per regions of interest.

The SNR optimization investigated in this work aimed to improve acquisition efficiency while accounting for practical limitations using radial acquisitions: total scan duration and SAR constraints.

The results demonstrated that acquisition optimization leads to a balance between image quality and acquisition time. Indeed, increasing the number of projections N_p generally improves signal quality but simultaneously extends scan duration. In human imaging, excessively long acquisitions are not optimal for the patient, and may increase the risk of motion, resulting in potential artifacts in the data.

Another important result about SNR optimization is that the range where the SNR is sufficiently high is characterized by relatively low repetition times. Indeed, the acquisition scan being set at 6 min 13 sec, the TR has to stay around 25 ms. If longer TR are used, the number of projections decreases and leads to SNR degradation.

This optimization method is then much more adapted to short-TR applications such as ultra-short echo time acquisition and simple acquisition for the diagnosis of diseases, such as multiple sclerosis, brain tumor or strokes [1]. In the case of T_2^* estimation, larger echo times are required to capture the full decaying signal, meaning that the repetition time must be larger. The optimization performed in this work was then not applicable for this type of acquisition, thus the latter require considerably increased total scan duration if similar image quality is required.

4.1.3 UTE and DARAD acquisition

The previous brain results were obtained using the density-adapted radial sequence encoding DARAD. Using such sampling density is advantageous in term of SNR and fitting accuracy because it increases the number of samples near the center of k-space. It allows to better capture the fast decaying signal of sodium isotope compared to the classic UTE sequence where the sampling density is constant all over the k-space.

The use of the DARAD sequence is therefore recommended over the conventional UTE sequence due to its improved performance in both T_1 and T_2^* mapping. The phantom experiments demonstrated that DARAD provides more robust parameter estimation, resulting in considerably narrower parameter distributions centered around a single relaxation value, as illustrated in Figures 3.16 and 3.19. This improved precision was further reflected in the corresponding T_1 and T_2^* maps, which exhibit a higher degree of spatial uniformity. For instance, the T_2^* maps obtained from UTE acquisitions showed noticeable spatial variations across the phantom regions. Such variations are not expected, as the phantoms were designed to be homogeneous and should therefore produce uniform maps of both signal amplitude S_0 and relaxation time. The presence of these inhomogeneities suggests reduced accuracy in the parameter estimation process. Conversely, the relaxation maps generated using the DARAD sequence displayed a much more homogeneous appearance, the observed spatial variations largely disappeared. These results indicate that DARAD encoding improves the reliability of quantitative sodium MRI measurements and provides parameter estimates that better reflect the true physical properties of the phantom.

This efficiency was already proved in terms of image quality in different researches [12, 18, 25] and the use of DARAD sequence is therefore necessary to reach better results.

4.2 Reliability of quantitative relaxation mapping

4.2.1 T_1 estimation

The estimation of T_1 relaxation times using the variable flip angle method produced relatively unstable results in both phantom and human brain experiments. Similarly to the estimation of T_2^* parameters, the fitting procedure exhibited sensitivity to noise but fewer boundary convergence issues compared to the case of T_2^* bi-exponential model. The resulting brain map displayed coherent anatomical structures in terms of signal amplitude, but were much less segmented considering the T_1 relaxation time map. Moreover, the mean value of T_1 in the brain was evaluated at 44.1 ms in the literature [15], which is lower than the mean measured value of 55 ms. This shows that the current method may not be the best in estimating T_1, highlighting the limitation of the model.

The variable flip angle method is known to be sensitive to flip angle inaccuracies and B_1 field inhomogeneities, particularly at ultra-high magnetic field strengths such as 7T. These effects may introduce systematic biases in the estimated relaxation times. This would be damped down if flip angle and B_1 inhomogeneity maps were generated in order to correct these variations for each voxel in the volume. Indeed, even if B_1 and flip angle are supposed to be constant all over the field of view, it is still technically impossible in practice because of hardware limitations. Accounting for some map corrections would then increase the accuracy of the prediction.

4.2.2 T_2^* estimation

The estimation of T_2^* relaxation parameters was even more challenging. The results consistently demonstrated a strong dependence on both acquisition quality and fitting models. The low SNR characteristic of sodium MRI amplifies fitting uncertainty, especially for parameters associated with the fast relaxation time signal fraction f.

However, one of the models used in this thesis looks quite good: the mono-exponential approximation model. Unfortunately, the signal decay fitted through a mono-exponential curve does not fully represent the reality in main brain tissues, but can be used without further approximation in liquid like structures such as CSF. The results obtained through this model are then biased and need to be analyzed with care. Despite this limitation, the range of estimated T_2^* values are coherent with the ones found in literature by Nagel [15] and Fleysher [26] both in the CSF and in the white and gray matter. This means that the mono-exponential modeling is in fact inaccurate considering the real behavior of sodium nuclei but its results are shown to be reproducible from what was already done by other researchers.

On the contrary, the experimental results based on bi-exponential fitting revealed substantial variability in the estimated relaxation parameters. Histograms of the fitted values showed broad distributions and accumulations near fitting boundaries, suggesting the presence of parameter instability in some regions caused by the high level of noise such as the one found in sodium MR images. These values do not seem relevant because of this instability and, as previously suggested, some improvements may be obtained by considering different regions of interest through the brain tissues in order to have more uniform sets of fitting curves. Even considering this approach, another problem stands: the multi-parametric fitting curve, inducing a large number of possible combinations between all 4 inter-dependent parameters of the bi-exponential model. A slight change from the theoretical decay curve induces errors in parameter estimation. Indeed, minimizing the mean squared error of the fit may not be the best way to evaluate which combination of parameters best physiologically represent the signal decay and should be carefully considered.

Another important point in parameter estimations is the choice of boundary values of the fitting components. In this work, boundaries were chosen to fit the physiological values found in literature at 7T but a lot of resulting estimations lead to accumulations of parameter values at these boundaries. Once again, this phenomenon is certainly induced by a too high level of noise in the data, making the model to try to fit the data even if they are not physiologically coherent and therefore, reaching the bound values.

Moreover, even if goodness-of-fit metric R^2 generally indicated precise fits, these results also demonstrated that high R^2 values do not necessarily guarantee physiologically meaningful parameter estimates. Additional validation criteria may therefore be required

to better interpret and evaluate the consistency of quantitative sodium T_2^* histograms maps.

These results indicate that quantitative T_2^* mapping remains one of the most demanding aspects of sodium MRI and requires careful optimization of both acquisitions, image quality and fitting procedures.

4.3 Mono- versus bi-exponential modeling

4.3.1 Findings from simulations

The simulated phantom experiments provided valuable information about the behavior of mono-exponential and bi-exponential fitting approaches under controlled conditions, allowing the estimation of the relative error made using both methods.

For mono-exponential model, the parameter estimation was generally stable and demonstrated relatively low variability even in the presence of realistic noise level. This behavior was indeed expected because few parameters must be estimated, reducing the sensibility of parameter variability and coupling.

On the contrary, the sensibility to noise and sampling conditions were much more important using bi-exponential model and are justified by the interdependency of the four parameters and a large parameter coupling. Reliable estimations of the fast, slow relaxation components and signal fraction required higher SNR and sufficiently large temporal range of sampling.

These affirmations highlight the trade-off between model complexity and physiological realism. In human brain tissues, mono-exponential model would be used in case of highly noised image and the errors should be taken into account when the bi-exponential model can be used when realistic evaluation of the transverse relaxation times is required. However, structures containing liquid, such as the CSF, must be described using a mono-exponential fitting due to the lack of ionic motion restrictions and then the averaging of the quadrupolar interactions of sodium nuclei with its environment.

4.3.2 Findings from human brain data

The observations obtained from the simulation experiments were partially confirmed in human brain data. The bi-exponential model provided a more detailed description of the measured signal decay and generally achieved higher goodness-of-fit values. However, the estimated parameters exhibited broader distributions and increased variability compared with the mono-exponential model. As previously noted, histograms of the fitted parameters revealed accumulations near fitting boundaries and voxel-to-voxel variability, indicating that parameter estimation remained sensitive to noise and acquisition limitations.

These findings suggest that while bi-exponential fitting better represents the physical behavior of sodium relaxation, its practical implementation remains considerably more difficult and challenging than mono-exponential fitting.

4.3.3 Practical implications

The choice between mono-exponential and bi-exponential fitting ultimately depends on the objectives of the study and the quality of the acquired data.

For routine quantitative mapping or acquisitions with limited SNR, the mono-exponential model will offer greater robustness and reproducibility. Although simplified, it provides stable estimates that may be sufficient for many practical applications. The bi-exponential model becomes advantageous when the objective is to investigate tissue microstructures or characterize distinct sodium environments. In the case of the evaluation of the relaxation properties in precise regions of the brain, this model should be prioritized. However, the successful application of bi-exponential fitting requires the optimization of acquisition protocols and sufficient image quality to ensure reliable parameter estimation.

The results obtained in this thesis therefore suggest that bi-exponential modeling remains primarily a research tool, whereas mono-exponential fitting may offer a more practical solution for routine quantitative sodium MRI.

4.4 Limitations and perspectives

Although the results obtained in this thesis demonstrate the feasibility of quantitative sodium MRI at 7T, several limitations should be considered when interpreting the findings and assessing their applicability.

The most significant limitation arises from the intrinsically low SNR of sodium MRI. Unlike conventional ^{1}H MRI, sodium imaging suffers from a substantially lower gyromagnetic ratio and lower tissue concentration, resulting in reduced signal intensity. In addition, the rapid transverse relaxation of sodium leads to further signal loss sometimes before data acquisition can be captured. Even using ultra-high field imaging and optimized acquisition strategies, SNR remained the major limitation of this work. It was particularly evident during the estimation of multi-component transverse relaxation parameters, where noise strongly affected fitting stability and reproducibility. As demonstrated by both simulations and experimental results, small variations in signal quality can lead to large variations in the estimated bi-exponential parameters.

Another limitation concerns the relatively small number of human datasets included in this study. In fact, the dataset size does not allow robust conclusions regarding biological variability across subjects. Quantitative sodium MRI parameters may be influenced by several physiological factors, including hydration status, tissue relaxation properties and individual anatomical differences. Consequently, the results obtained in this work should primarily be considered as a methodological and modeling validation rather than a determination of sodium relaxation properties in the general population. Increasing the size of the human dataset would strengthen the proof of concept presented in this work and would improve the statistical robustness of the results, increase confidence in the proposed methods, and allow a better assessment of its reproducibility. However, acquiring data from a large number of healthy volunteers was beyond the scope and time constraints of this master's thesis. Future studies involving larger populations would therefore be valuable to further validate this approach and assess its applicability across a broader range of subjects.

The phantom experiments also present limitations. Although phantoms provide a relatively controlled environment for validating acquisition and fitting procedures, they cannot fully reproduce the complexity of biological tissues. The sodium-containing gels used in this work represent environments with unrestricted ionic motion and homogeneous relaxation properties. In contrast, biological tissues contain highly heterogeneous intracellular and extracellular compartments and varying degrees of molecular restriction. Therefore, the behavior of the fitting procedures observed in phantoms underestimate some of the challenges encountered *in vivo*. The use of more advanced phantoms incorporating different compartments, gels of different sodium relaxation properties and concentration could provide a more realistic framework for future studies.

Several methodological problems should also be acknowledged. The quantitative mapping relied essentially on voxel-wise fitting approaches, which treat each voxel independently. While this strategy is simple to implement and interpret, it does not exploit spatial information that may help to stabilize parameter estimation in low-SNR conditions. Consequently, some regions exhibited noisy parameter estimates and increased variability. In addition, the bi-exponential fitting model introduces potential sources of uncertainty. The presence of broad parameter distributions and boundary-constrained estimates observed in the results suggests that these issues remain relevant even when R^2 values appear satisfactory.

Another important methodological problem stems from the fact that relaxation parameters were optimized by minimizing the mean squared error (MSE) between the measured signal and the fitted model. Although MSE is useful for finding the best fit, it only measures how well the model matches the data. A low MSE does not necessarily mean that the estimated parameters are accurate or physiologically reliable, especially for bi-exponential fitting where different parameter combinations can produce very similar curves. To better evaluate the quality of the estimated parameters, additional methods could be used. For example, confidence intervals would provide information about the uncertainty of each parameter, or Monte Carlo simulations could assess the robustness to noise. These approaches would complement the MSE and provide a more complete evaluation of the fitting performance.

Furthermore, the estimation of R^2 may not be the most adapted method to evaluate the accuracy of the fit. Indeed, even if the fit reproduces the measured signal decay, it does not necessarily reflect the reliability or physiological plausibility of the estimated parameters. In multiple component models, different parameter combinations may produce very similar signal curves and therefore comparable R^2 values. As a result, a fit may exhibit a high R^2 even if unstable, boundary-constrained, or not physiologically realistic parameter estimations. Consequently, this metric should be interpreted in addition to other indicators of fitting quality and robustness. Future studies could complement R^2 analysis with residual analysis, RMSE, and model selection criteria such as AIC [27] which may provide a more comprehensive assessment of fitting quality and model accuracy, particularly when comparing mono-exponential and bi-exponential relaxation models.

Another important limitation concerns the absence of explicit corrections for magnetic field and excitation flip angle inhomogeneities. At ultra-high magnetic field strengths such as 7T, both B_0 and B_1 field variations can significantly affect image quality and estimation accuracy. In particular, spatial variations in the transmitted RF field may lead to discrepancies between nominal and effective flip angles, potentially introducing systematic bias in variable flip angle T_1 measurements. The absence of dedicated field correction procedures may have contributed to inaccuracies in the estimated relaxation values and

should be included for further researches.

Finally, the biological interpretation of sodium relaxation parameters remains inherently complex. While the fast and slow components estimated through bi-exponential fitting are often associated with sodium populations in different motional environments, these parameters cannot be directly assigned to specific physiological compartments. The measured relaxation behavior reflects a combination of multiple microscopic processes, including molecular interactions, tissue architecture, and ion mobility [28]. Therefore, particular caution should be taken when drawing physiological conclusions solely from fitted relaxation parameters.

4.5 Discussion summary

The results presented in this work demonstrate that quantitative sodium MRI at 7T is feasible but remains strongly influenced by the intrinsic limitations of sodium imaging, particularly low SNR and rapid signal decay. The simulation and experimental studies highlighted the importance of acquisition design, echo sampling strategy, and fitting methodology for obtaining reliable relaxation parameter estimates.

While the variable flip angle method provided unstable T_1 estimations, T_2^* mapping was proved even more challenging, especially when using bi-exponential fitting approaches. The comparison between mono- and bi-exponential models revealed a trade-off between robustness and physiological realism, suggesting that the choice of model should be guided by both the quality of the acquired data and the objectives of the study.

Overall, these findings emphasize the need for continued improvements in acquisition protocols and quantitative analysis methods to further enhance the reliability of quantitative sodium MRI.

Chapter 5

Conclusion

The objective of this thesis was to investigate the feasibility of quantitative sodium MRI at 7T with the estimation of longitudinal and transverse relaxation parameters in phantoms and human brains. Given the intrinsically low signal-to-noise ratio (SNR) of ^{23}Na MRI and the rapid decaying signal caused by quadrupolar interactions, special attention was devoted to the optimization of image acquisition and the choice of the fitting procedures.

A first contribution of this work was the optimization of acquisition parameters under realistic constraints on acquisition time and specific absorption rate (SAR). By expressing the SNR as a function of repetition time while keeping constant SAR and scan duration, an optimized set of sequence parameters composed of repetition time, flip angle and number of projections in k-space, was identified and experimentally validated. The acquisitions demonstrated improved image quality and confirmed the relevance of the proposed optimization framework for sodium MRI.

Then, quantitative mapping of sodium relaxation parameters was explored through the estimation of T_1 and T_2^* relaxation times. Relaxation maps were generated from both phantom and human brain data, demonstrating the possibility to generate quantitative sodium MRI at ultra-high field. In addition, UTE and DARAD acquisition strategies were compared, and the use of radial acquisition was shown to be much more accurate both in parameter estimations and global homogeneity of the acquired images. Mono-exponential and bi-exponential models were evaluated for the characterization of sodium signal decay in human brain and the results show that mono-exponential model allows more stable T_2^* estimation, while the bi-exponential one presented lower accuracy in the multi-parametric estimation. Consequently, quantitative ^{23}Na MRI can provide information beyond conventional hydrogen imaging and may contribute to a better understanding of tissue properties.

However, this study has some limitations. The number of volunteers was relatively small, which limits the evaluation of reproducibility and inter-subject variability. In addition, the fitting procedures were mainly evaluated using the mean squared error, which does not fully describe the uncertainty of the estimated parameters. Future work could include larger cohorts and additional statistical tools, such as confidence intervals or Monte Carlo simulations, to better assess the reliability of the measurements.

Overall, this thesis contributes to the development of quantitative sodium MRI at 7T and highlights its potential for the assessment of tissue relaxation properties in the human brain.

Declaration of Artificial Intelligence use

Artificial intelligence tools were used to assist with english writing, report structure and code debugging. However, all the scientific contents, interpretations and conclusions remains the responsibility of the author.

Bibliography

1. Madelin G, Lee JS, Regatte RR, and Jerschow A. Sodium MRI: Methods and applications. Progress in nuclear magnetic resonance spectroscopy 2014 May; 79:14–47. DOI: 10.1016/j.pnmrs.2014.02.001. Available from: https://pmc.ncbi.nlm.nih.gov/articles/PMC4126172/ [Accessed on: 2026 Mar 17]
2. Sodium — Facts, Uses, & Properties — Britannica. en. 2026 Mar. Available from: https://www.britannica.com/science/sodium [Accessed on: 2026 Mar 31]
3. Titze J. A different view on sodium balance. Current opinion in nephrology and hypertension 2015; 24:14–20
4. Pirahanchi Y, Jessu R, and Aeddula NR. Physiology, Sodium Potassium Pump. eng. *StatPearls*. Treasure Island (FL): StatPearls Publishing, 2026. Available from: http://www.ncbi.nlm.nih.gov/books/NBK537088/ [Accessed on: 2026 Mar 17]
5. Adlung A, Licht C, Reichert S, Özdemir S, Mohamed SA, Samartzi M, Fatar M, Gass A, Prost EN, and Schad LR. Quantification of tissue sodium concentration in the ischemic stroke: A comparison between external and internal references for 23Na MRI. Journal of Neuroscience Methods 2022 Dec; 382:109721. DOI: 10.1016/j.jneumeth.2022.109721. Available from: https://www.sciencedirect.com/science/article/pii/S0165027022002473 [Accessed on: 2026 Apr 16]
6. Huhn K, Engelhorn T, Linker RA, and Nagel AM. Potential of Sodium MRI as a Biomarker for Neurodegeneration and Neuroinflammation in Multiple Sclerosis. Frontiers in Neurology 2019 Feb; 10:84. DOI: 10.3389/fneur.2019.00084. Available from: https://pmc.ncbi.nlm.nih.gov/articles/PMC6378293/ [Accessed on: 2026 Mar 17]
7. Regnery S, Behl NG, Platt T, Weinfurtner N, Windisch P, Deike-Hofmann K, Sahm F, Bendszus M, Debus J, Ladd ME, et al. Ultra-high-field sodium MRI as biomarker for tumor extent, grade and IDH mutation status in glioma patients. NeuroImage: Clinical 2020; 28:102427
8. Shellock FG. Radiofrequency energy-induced heating during MR procedures: a review. Journal of Magnetic Resonance Imaging 2000; 12:30–6
9. Okada T, Akasaka T, Thuy DH, and Isa T. Safety for Human MR Scanners at 7T. Magnetic Resonance in Medical Sciences 2021 Aug; 21:531–7. DOI: 10.2463/mrms.rev.2021-0063. Available from: https://pmc.ncbi.nlm.nih.gov/articles/PMC9618930/ [Accessed on: 2026 May 19]
10. Peters AM, Brookes MJ, Hoogenraad FG, Gowland PA, Francis ST, Morris PG, and Bowtell R. T2* measurements in human brain at 1.5, 3 and 7 T. Magnetic resonance imaging 2007; 25:748–53

11. Ridley B, Nagel AM, Bydder M, Maarouf A, Stellmann JP, Gherib S, Verneuil J, Viout P, Guye M, Ranjeva JP, and Zaaraoui W. Distribution of brain sodium long and short relaxation times and concentrations: a multi-echo ultra-high field 23Na MRI study. en. Scientific Reports 2018 Mar; 8:4357. DOI: 10.1038/s41598-018-22711-0. Available from: https://www.nature.com/articles/s41598-018-22711-0 [Accessed on: 2026 Mar 17]

12. Nagel AM, Laun FB, Weber MA, Matthies C, Semmler W, and Schad LR. Sodium MRI using a density-adapted 3D radial acquisition technique. en. Magnetic Resonance in Medicine 2009; 62. _eprint: https://onlinelibrary.wiley.com/doi/pdf/10.1002/mrm.22157:1 73. DOI: 10.1002/mrm.22157. Available from: https://onlinelibrary.wiley.com/doi/abs/10.1002/mrm.22157 [Accessed on: 2026 Apr 1]

13. Karakuzu A, Boudreau M, Duval T, Boshkovski T, Leppert I, Cabana JF, Gagnon I, Beliveau P, Pike GB, Cohen-Adad J, et al. qMRLab: Quantitative MRI analysis, under one umbrella. Journal of Open Source Software 2020; 5

14. Coste A, Boumezbeur F, Vignaud A, Madelin G, Reetz K, Le Bihan D, Rabrait-Lerman C, and Romanzetti S. Tissue sodium concentration and sodium T1 mapping of the human brain at 3 T using a Variable Flip Angle method. Magnetic resonance imaging 2019 May; 58:116–24. DOI: 10.1016/j.mri.2019.01.015. Available from: https://pmc.ncbi.nlm.nih.gov/articles/PMC6927040/ [Accessed on: 2026 May 4]

15. Nagel AM, Schmitter S, Bock M, Moser E, Semmler W, and Schad LR. Parameter Optimization for 7T 23Na-MRI. en

16. Weiskopf N, Suckling J, Williams G, Correia MM, Inkster B, Tait R, Ooi C, Bullmore ET, and Lutti A. Quantitative multi-parameter mapping of R1, PD*, MT, and R2* at 3T: a multi-center validation. Frontiers in neuroscience 2013; 7:95

17. Relaxometry Series: Variable Flip Angle — qMRLab. Available from: https://qmrlab.org/jekyll/2018/12/11/T1-mapping-variable-flip-angle.html [Accessed on: 2026 Mar 17]

18. Nowikow C, Schulte RF, Vaeggemose M, Laustsen C, and Noseworthy MD. Signal-to-noise ratio comparison of k-space sampling schemes for sodium MRI of the brain at 3 T. eng. Magma 2026 Apr. DOI: 10.1007/s10334-026-01364-5

19. McCann AJ, Workman A, and McGrath C. A quick and robust method for measurement of signal-to-noise ratio in MRI. en. Physics in Medicine & Biology 2013 May; 58:3775. DOI: 10.1088/0031-9155/58/11/3775. Available from: https://doi.org/10.1088/0031-9155/58/11/3775 [Accessed on: 2026 Mar 31]

20. Human Neuroimaging WC for. Statistical Parametric Mapping (SPM12). Available at: https://www.fil.ion.ucl.ac.uk/spm/software/spm12/. Accessed: June 2026. 2024

21. Bazin PL, Alkemade A, Van der Zwaag W, Caan M, Mulder M, and Forstmann BU. Denoising high-field multi-dimensional MRI with local complex PCA. Frontiers in neuroscience 2019; 13:1066

22. SciPy Developers. scipy.optimize.dual_annealing. https://docs.scipy.org/doc/scipy/reference/generated/scipy.optimize.dual_annealing.html. Accessed: 2026-06-06. 2025

23. Qian Y, Lin YC, Chen X, Ge Y, Lui YW, and Boada FE. Single-quantum sodium MRI at 3 T for separation of mono- and bi-T2 sodium signals. en. Scientific Reports 2025 Jul; 15:27427. DOI: 10.1038/s41598-025-07800-1. Available from: https://doi.org/10.1038/s41598-025-07800-1 [Accessed on: 2026 Mar 17]

24. Qian Y, Zhao T, Zheng H, Weimer J, and Boada FE. High-resolution sodium imaging of human brain at 7 T. Magnetic resonance in medicine 2012; 68:227–33

25. Nielles-Vallespin S, Weber MA, Bock M, Bongers A, Speier P, Combs SE, Wöhrle J, Lehmann-Horn F, Essig M, and Schad LR. 3D radial projection technique with ultrashort echo times for sodium MRI: Clinical applications in human brain and skeletal muscle. en. Magnetic Resonance in Medicine 2007; 57. _eprint: https://onlinelibrary.wiley.com/doi/ 81. DOI: 10.1002/mrm.21104. Available from: https://onlinelibrary.wiley.com/doi/abs/10.1002/mrm.21104 [Accessed on: 2026 Mar 17]

26. Fleysher L, Oesingmann N, Stoeckel B, Grossman RI, and Inglese M. Sodium Long-Component T2 Mapping in Human Brain at 7 Tesla. Magnetic resonance in medicine : official journal of the Society of Magnetic Resonance in Medicine / Society of Magnetic Resonance in Medicine 2009 Nov; 62:1338–41. DOI: 10.1002/mrm.22133. Available from: https://pmc.ncbi.nlm.nih.gov/articles/PMC2790724/ [Accessed on: 2026 Apr 24]

27. Luypaert R, Ingrisch M, Sourbron S, and De Mey J. The Akaike information criterion in DCE-MRI: does it improve the haemodynamic parameter estimates? Physics in medicine and biology 2012; 57:3609–28

28. Syeda W, Blunck Y, Kolbe S, Cleary JO, and Johnston LA. A continuum of components: Flexible fast fraction mapping in sodium MRI. Magnetic resonance in medicine 2019; 81:3854–64